

Scientific Spokesperso
F.E. Taylor
Physics Department
North. Ill. Univ.
DeKalb, IL 60115
Phone (815) 753-1773

Proposal to Study Nucleon Structure Functions at High Q^2

D. Bogert, R. Brock, R. Fisk, T. Ohlka, L. Stutte, J.K. Walker, J. Wolfson
Fermi National Accelerator Laboratory
Batavia, IL

J. Bofill
~~R. Burg~~, W. Busza, J. Friedman, M. Goodman, H. Kendall,
T. Lyons, T. Mattison, L. Osborne, L. Rosenson,
M. Tartaglia, S. Whitaker, G.P. Yeh
Massachusetts Inst. of Technology
Cambridge, MA

M. Abolins, A. Cohen, J. Ernwein, D. Owen, J. Slate
Michigan State University
East Lansing, MI

F.E. Taylor
Northern Illinois University
DeKalb, IL

Table of Contents

I)	Introduction
II)	Structure Functions-Theoretical Formulation
a)	Basic quark model theory
b)	QCD corrections to deep inelastic scattering
III)	Experimental Interpretation
a)	Test 1 - The ratio test
b)	Test 2 - Extraction of structure functions.
IV)	Design of the experiment
a)	Method
b)	Resolutions
c)	Beam energy
V)	Event rates
VI)	Monte Carlo Simulation
a)	Method
b)	Results
VII)	Requests
VIII)	Conclusions
	References
	Figure captions and figures
	Appendix A - The apparatus

Proposal to Study
Nucleon Structure Functions at High Q^2

Abstract

The ultra small distance structure of the nucleon is to be measured by studying high energy deep inelastic neutrino-nucleon scattering in the Flash Chamber - Proportional Tube calorimeter located in Lab C. The fine grained sampling of this detector allows both the energy and angle of energy flow of the recoil showers to be determined. Thus the structure functions of both neutral current and charged current interactions can be measured. These measurements enable a determination of:

- 1) The Lorentz structure of the weak neutral current.
- 2) The Q^2 evolution of the structure functions up to high Q^2 .

This will test gauge theories of electro weak interactions and confront the QCD theory of strong interactions in a new high energy range.

Nucleon Structure Functions at High Q^2

P 649 : FNAL, MIT, MSU,
N. Ill. Univ.

I) Introduction:

We propose measuring the nucleon structure to ultra small distances by studying high energy deep inelastic neutrino - nucleon scattering in the Lab C Flash Chamber - Proportional Tube Calorimeter. The High Q^2 region $\lesssim 400$ (GeV/c) 2 unveiled by the Tevatron will allow structure in the range $\sim 10^{-2}$ fermi to be explored.

With the fine grained shower sampling capability of the Lab C detector, it is possible to measure both the energy as well as the direction of the recoiling hadron shower. This allows a complete reconstruction of the kinematics of both charged current and neutral current deep inelastic neutrino scattering in the narrow band neutrino beam. Hence the Lab C detector can determine the scaling variables $x = Q^2/2 m_p E_h$ and $y = E_h/E_\nu$ for both of these interactions.

A measurement of the four deep inelastic cross sections: $\frac{d\sigma}{dx dy}$
(-) (-)
($\bar{\nu}_\mu + N \rightarrow \bar{\nu}_\mu + x$) and $\frac{d\sigma}{dx dy}$ ($\bar{\nu}_\mu + N \rightarrow \mu^\pm + x$) (N=nucleon-isoscalar target) at the highest possible range of Q^2 , x and y , will enable the following tests of our understanding of weak and strong interactions:

1) A comparison of the Lorentz structure of the neutral current interaction at high center of mass energies ($W \sim 30$ GeV) with that at low energies will extend the tested range of gauge theories. In particular this will allow a determination of $\sin^2 \theta_w$ of the Weinberg-Salam theory in a new high energy regime.

2) A measurement of the Q^2 evolution of the structure functions F_2 and xF_3 for both neutral current and charged current interactions up to high $Q^2 \sim 400 \text{ (GeV/c)}^2$ is an excellent test of the currently popular QCD theory of strong interactions. Furthermore, a detailed comparison of the neutral current structure functions with the charged current structure functions tests that the nucleon structure is independent of the probe and gives a sensitivity to small differences in the strange and charm sea of the nucleon.

Experimentation at FNAL and the SPS has shown that violations to Bjorken scaling at large Q^2 are consistent with the predictions of QCD. However various theoretical ambiguities exist in an interpretation of the data. First order terms in QCD to determine α_s , the strength of the strong interaction coupling constant, are ambiguous to a scale factor. Second order terms must be included to determine the scale of the Q^2 dependence of α_s . This requires experiments at high Q^2 . Comparisons of the data at low Q^2 with the QCD theory have further difficulties of interpretation. Higher twist effects can account for the scale violations at low Q^2 . These effects are very poorly understood but are believed to fall with increasing Q^2 as an inverse power of Q^2 . Hence only high $Q^2 \gtrsim 10 \text{ to } 20 \text{ (GeV/c)}^2$ data can be used to unambiguously confront the QCD theory.^{1, 2}

Various probes can be used to study the small scale structure of the nucleon. The probe can be a virtual photon in deep inelastic electron or muon scattering. This probe couples to the charges of the quarks and has a $1/Q^4$ propagator dependence which gives a large suppression at high Q^2 . Only two structure functions of the nucleon

are determined by this type of experiment. For deep inelastic neutrino scattering, because of the large mass of the exchanged W^\pm boson in charged currents or the Z^0 boson in neutral currents, one expects almost no propagator effects at finite Q^2 . ($Q^2 \lesssim 400$ (GeV/c) 2 propagator effects are $\sim 10\%$). Hence the scattering cross section does not have the strong falloff at large Q^2 . Furthermore, since parity is violated in the weak interaction, there are three structure functions in the deep inelastic scattering cross sections which enable one to directly probe the valence quark structure of the nucleon.

Although the structure of the nucleon is believed to be independent of the probe, (good evidence exists in, ~~in~~ ⁱⁿ ~~versus~~ ⁱⁿ charged currents) model independent checks of this assumption can be made with an experiment which can simultaneously measure the nucleon structure functions as probed by the neutral current with those which are probed by the charged current. Subtle differences are expected to exist between the structure functions of these two probes, which depend on the difference between the charm and strange quark sea.³

At this time, it is believed that there are 6 point-like quarks; 5 quark flavors have been detected and the 6th quark is being intensely searched for. There are many questions about the fundamental structure of matter. Why are there different flavor quarks? Is there another level of structure of matter - a subquark which is used to build quarks? Is color an exact symmetry? Can color be excited and fractionally charged quarks be resolved into

integrally charged quarks of different colors? A subquark structure would give rise to an enhancement of $d\sigma/dx dy$ in the low x region at high Q^2 . A color excitation would make the deep inelastic cross section rise at large Q^2 . These questions demand further experimentation at the highest Q^2 . Since the Tevatron will allow a new high range of Q^2 and W to be explored, there is the exciting possibility that some fundamental revelation in our understanding of the structure of matter will occur.

II) Structure Functions - Theoretical Formulation

In this section we present the theoretical formulation of deep inelastic neutrino - nucleon scattering for both the charged current and the neutral current interactions. We will use this formulation to simulate the response of the detector to neutrino events in the narrow band beam.

a) Basic quark model theory:

A neutrino (antineutrino) may interact with a nucleon by exchanging charged heavy bosons W^\pm , or a neutral heavy boson Z^0 . In the quark-parton model of the nucleon, this scattering process takes place by the heavy gauge boson interaction with one of the quarks inside the nucleon. These processes are depicted in figure 1. The charged current is flavor changing and pure V-A, and the neutral current is believed to be flavor diagonal to a good approximation and contains a mixture of V-A and V+A amplitudes.

The Lagrangian for the charged current interaction as given in the standard notation of the quark model is:

$$L^{cc} = \frac{-G}{\sqrt{2}} \gamma_\alpha (v \gamma_\alpha (1 + \gamma_5) u) (\bar{d} c \gamma_\alpha (1 + \gamma_5) u) + h.c. \quad (1)$$

where G is the universal fermi constant = $1.17 \times 10^{-5} \text{ GeV}^{-2}$ and $dc = d \cos \theta_c + s \sin \theta_c$, θ_c = Cabibbo angle, and $u(x)$ is the probability that a u flavor quark has a momentum fraction x of the nucleon momentum, etc.

In the $SU(2) \times U(1)$ gauge theory of Weinberg-Salam there are two components to the neutral current: the photon and the Z^0 boson. These two amplitudes are mixed by an angle θ_w . Hence the neutral current Lagrangian is given by (in the notation of Sakurai and Hung⁴ (assuming no flavor changing neutral currents):

$$L^{nc} = \frac{-G}{2} \bar{v} \gamma_\lambda (1 + \gamma_5) v \left\{ 1/2 [\bar{u} \gamma_\lambda (\alpha + \beta \gamma_5) \bar{u} - \bar{d} \gamma_\lambda (\alpha + \beta \gamma_5) d] \right. \quad (2)$$

$$+ 1/2 [\bar{u} \gamma_\lambda (\gamma + \delta \gamma_5) u + \bar{d} \gamma_\lambda (\gamma + \delta \gamma_5) d] + \bar{s} (\gamma' + \delta' \gamma_5) s$$

$$+ \text{possible } \bar{c}c, \bar{t}t, \bar{b}b \text{ terms} \} .$$

For pure V-A, $\alpha = \beta$, and $\gamma = \delta$, but in general we have in the W.S. model:

$$\alpha = 1 - 2 \sin^2 \theta_w \quad \beta = 1$$

(isovector-vector) (isovector - axial vector) (3a)

$$\gamma = -2/3 \sin^2 \theta_w \quad \delta = 0$$

(isoscalar - vector) (isoscalar - axial vector) (3b)

and with the GIM mechanism:

$$\gamma' = -1/2 + 2/3 \sin^2 \theta_w, \quad (3c)$$

$$\delta' = -1/2 \quad (3d)$$

Thus the neutral current interaction is in general not pure V-A since $\sin^2 \theta_w \neq 0$.

These interactions lead to the following cross sections for an isoscalar target.³ (The threshold effects for charm production and quark flavors beyond charm are neglected). For charged currents:

$$\left(\frac{d\sigma}{dx dy} \right)_{cc}^{\nu_\mu} = \frac{G^2 m E_\nu}{\pi} \left\{ [xq(x) + xs(x) - xc(x)] + (1-y)^2 [x\bar{q}(x) + x\bar{c}(x) - x\bar{s}(x)] \right\} \quad (4)$$

and

$$\left(\frac{d\sigma}{dx dy} \right)_{cc}^{\bar{\nu}_\mu} = \frac{G^2 m E_\nu}{\pi} \left\{ [x\bar{q}(x) + x\bar{s}(x) - x\bar{c}(x)] + (1-y)^2 [xq(x) + xc(x) - xs(x)] \right\} \quad (5)$$

For neutral currents:

$$\begin{aligned} \left(\frac{d\sigma}{dx dy} \right)_{nc}^{\nu_\mu} = \frac{G^2 m E_\nu}{\pi} \left\{ \right. & xV(x) [\delta_1^2 + \delta_2^2 + (\delta_3^2 + \delta_4^2)(1-y)^2] \\ & + (x\bar{u}(x) + x\bar{d}(x)) [\delta_1^2 + \delta_2^2 + \delta_3^2 + \delta_4^2] (1+(1-y)^2) \\ & + (xs(x) + x\bar{s}(x)) [\delta_2^2 + \delta_4^2] (1 + (1-y)^2) \\ & \left. + (xc(x) + x\bar{c}(x)) [\delta_1^2 + \delta_3^2] (1 + (1-y)^2) \right\} \quad (6) \end{aligned}$$

and

$$\begin{aligned} \frac{d\sigma}{dx dy} \frac{\bar{\nu}_\mu}{nc} &= \frac{G^2 m E_\nu}{\pi} \left\{ x v(x) [(\delta_1^2 + \delta_2^2) (1-y)^2 + (\delta_3^2 + \delta_4^2) \right. \\ &+ (x \bar{u}(x) + x \bar{d}(x)) [\delta_1^2 + \delta_2^2 + \delta_3^2 \delta_4^2] (1 + (1-y)^2) \\ &+ (x s(x) + x \bar{s}(x)) [\delta_2^2 + \delta_4^2] (1 + (1-y)^2) \\ &+ (x c(x) + x \bar{c}(x)) [\delta_1^2 + \delta_3^2] (1 + (1-y)^2) \end{aligned} \quad (7)$$

$$\text{where:} \quad \delta_1 = 1/2 - 2/3 \sin^2 \theta_w = u_L = 1/4 (\alpha + \beta + \gamma + \delta) \quad (8a)$$

$$\delta_2 = -1/2 + 1/3 \sin^2 \theta_w = d_L = 1/4 (\gamma - \alpha + \delta - \beta) \quad (8b)$$

$$\delta_3 = -2/3 \sin^2 \theta_w = u_R = 1/4 (\alpha + \gamma - \beta - \delta) \quad (8c)$$

$$\delta_4 = 1/3 \sin^2 \theta_w = d_R = 1/4 (\gamma + \beta - \alpha - \delta) \quad (8d)$$

and

$$V(x) = u_V(x) + d_V(x) = q(x) - \bar{q}(x)$$

$$q(x) = \sum_i q_i(x), \quad \bar{q}(x) = \sum_i \bar{q}_i(x)$$

These cross sections may be written in terms of the familiar structure functions F_1, F_2, F_3 as follows:

$$\frac{d\sigma}{dx dy} \frac{\nu}{v} = \frac{G^2 m E_\nu}{\pi} \left\{ (1-y) F_2(x, Q^2) + xy^2 F_1(x, Q^2) + (1-\frac{y}{2}) xy F_3(x, Q^2) \right\} \quad (9)$$

Neglecting quark transverse momentum and assuming the Callen-Gross relation⁵. ($2xF_1=F_2$) we form the following table of structure functions in terms of the scaled quark and antiquark momentum distributions.

Table I

	charged current	neutral current
F_2^{ν}	$x\Sigma(x) = xq(x) + x\bar{q}(x)$	$x\Sigma(x) [\delta_1^2 + \delta_2^2 + \delta_3^2 + \delta_4^2]$ $+ x\Delta^N(x) [\delta_1^2 + \delta_3^2 - \delta_2^2 - \delta_4^2]$
xF_3^{ν}	$xV(x) \mp x\Delta^N(x)$ $= xq(x) - x\bar{q}(x) \mp (x\bar{c}(x) - x\bar{s}(x) + xc(x) - xs(x))$	$xV(x) [\delta_1^2 + \delta_2^2 - \delta_3^2 - \delta_4^2]$

We note that xF_3 is for both neutral current and charged current interactions a flavor nonsinglet and is a measure of the valence quark x distribution. On the other hand F_2 for charged currents is a pure flavor singlet, the neutral current, however, contains both a singlet ($x\Sigma$) and a non-singlet term ($x\Delta^N$) (expected to be small) and measures the total quark distribution.

b) QCD corrections to deep inelastic scattering

Quantum chromodynamics (QCD) is an $SU(3)_c$ color gauge theory which models the interactions between quarks and gluons - the mediator of the strong interaction. In this theory, quarks are arranged in color triplets and have distinct flavors. The strong

coupling constant $\alpha_s(Q^2)$ becomes weaker at high Q^2 due to an anti-shielding of the gluon field around the bare quark color charge. This antishielding makes perturbation calculations of the theory more reliable at high Q^2 .

Holding Q^2 fixed and measuring the structure functions versus x , determines the nucleon structure at a given distance scale. When a Z^0 or W^\pm boson strikes a quark at ever increasing Q^2 , and thus at ever smaller distances, a quark can be resolved into a quark plus a gluon, and a gluon into a quark-antiquark pair or a gluon pair. These radiative corrections to a quark or a gluon are depicted in figure 2. Hence the scaled quark, and antiquark momentum distributions will depend on Q^2 . Since these radiative processes tend to soften the hard boson-quark scattering at high Q^2 , one would expect the large $x \gtrsim 0.4$ values of the structure functions F_2 and xF_3 to decrease and the small $x \lesssim 0.2$ values to increase with increasing Q^2 . This qualitative behavior has been verified by extensive experimentation.

The Q^2 evolutions of the singlet structure function $F_2(x, Q^2)$ and the nonsinglet structure function $xF_3(x, Q^2)$ are expected to be different. To leading order, xF_3 can evolve by only gluon radiation (figure 2a), whereas $F_2(x, Q^2)$ is sensitive to both gluon radiation and quark-antiquark pair production (figure 2b) as well as indirectly dependent on the triplet gluon process (figure 2c). Hence $F_2(x, Q^2)$ at small x is expected to grow with increasing Q^2 more rapidly than $xF_3(x, Q^2)$.

The behavior of $xF_3(x, Q^2)$ does not provide an incisive test to distinguish between different theories of strong interactions, but does provide a necessary consistency check of QCD. However the singlet structure function $F_2(x, Q^2)$ can distinguish between different theories by the Q^2 behavior of the $n=2$ moment:

$$\int_0^1 F_2(x, Q^2) dx = \langle x \Sigma(Q^2) \rangle_2$$

Only QCD predicts that this moment should decrease with increasing Q^2 . Since this behavior is consistent with experimental data, certain other proposed theories are excluded.⁶

QCD makes predictions on the moments of the structure functions F_2 and xF_3 . These have been extensively measured and compared with good agreement to theoretical predictions. However, certain ambiguities remain in the interpretation of these data. These ambiguities involve extending the theory to low Q^2 . What remains to be measured? There are several contributions that a Tevatron experiment can make:

- 1) Measure the Q^2 evolution of F_2 and xF_3 up to the very highest value of Q^2 . Higher twist terms should be small and thus the theory can be directly tested.

- 2) Compare the neutral current structure functions with the charged current structure functions. This tests that the structure functions are independent of the probe and checks that the $x\Delta^n(x)$ term is small.

3) Estimate the value of $R = F_L/F_2$, ($F_L(x, Q^2) = F_2(x, Q^2) - 2xF_1(x, Q^2)$) as a function of x for various values of Q^2 . This ratio is sensitive to the triple gluon vertex. Since F_2 alone has little sensitivity to the triple gluon vertex there are few other ways of measuring this important aspect of the theory. The measurement of this quantity is very difficult, however.

III) Experimental Interpretation

The simultaneous measurement of $\frac{d\sigma}{dx dy} (\bar{\nu}_{\mu} + N \rightarrow \bar{\nu}_{\mu} + x)$ (neutral current) and $\frac{d\sigma}{dx dy} (\nu_{\mu} + N \rightarrow \mu^{\pm} + x)$ (charged current) will allow a determination of:

- 1) The couplings $(\delta_1^2 + \delta_2^2)$ and $(\delta_3^2 + \delta_4^2)$ and thus the Weinberg angle.
- 2) The structure functions $F_2(x, Q^2)$, $xF_3(x, Q^2)$ for both the neutral current and the charged current interaction.

To extract the information above, we formulate two tests of the data. The emphasis is on the x distribution of the neutral current, which to date has been rather poorly measured.^{7, 8}

a) Test 1

The ratios of the neutral current cross sections to the charged current cross sections determine the couplings $(\delta_1^2 + \delta_2^2)$ and $(\delta_3^2 + \delta_4^2)$. This determination is independent of uncertainties in the incident neutrino flux. Any deviation of these ratios from a constant indicates the presence of the antiquark sea or unexpected structure in the neutral and/or charged current propagators at large Q^2 .

Neglecting strange and charm quarks, and separately integrating the numerator and denominator over y we have:

$$R^{\nu}_{\mu}(x) = \frac{\frac{d\sigma}{dx}^{\nu}_{\mu}(nc)}{\frac{d\sigma}{dx}^{\nu}_{\mu}(cc)} = a + \frac{x\bar{q}(x) \cdot 4/3 (b-a)}{xq(x) + 1/3 x\bar{q}(x)} \quad (10a)$$

and:

$$R^{\bar{\nu}}_{\mu}(x) = \frac{\frac{d\sigma}{dx}^{\bar{\nu}}_{\mu}(nc)}{\frac{d\sigma}{dx}^{\bar{\nu}}_{\mu}(cc)} = 3\bar{a} + \frac{x\bar{q}(x) (4/3 b - 4\bar{a})}{1/3 x q(x) + x\bar{q}(x)} \quad (10b)$$

where:

$$a = \delta_1^2 + \delta_2^2 + 1/3 (\delta_3^2 + \delta_4^2)$$

$$\bar{a} = 1/3 (\delta_1^2 + \delta_2^2) + \delta_3^2 + \delta_4^2$$

$$b = \delta_1^2 + \delta_2^2 + \delta_3^2 + \delta_4^2$$

The values of these ratios at large x determine the couplings $(\delta_1^2 + \delta_2^2) = 3/8(3a - \bar{a})$ and $(\delta_3^2 + \delta_4^2) = 3/8(3\bar{a} - a)$ and hence, in the Weinberg-Salam model, the value of $\sin^2 \theta_w$. In terms of the coupling constants of Hung and Sakurai (equation 2), this ratio test gives:

$$\delta_1^2 + \delta_2^2 = 1/8 \left\{ (\alpha + \beta)^2 + (\gamma + \delta)^2 \right\} \quad \text{and}$$

$$\delta_3^2 + \delta_4^2 = 1/8 \left\{ (\alpha - \beta)^2 + (\gamma - \delta)^2 \right\} . \quad \text{Hence } \alpha^2 +$$

$\beta^2 + \gamma^2 + \delta^2$, and $\alpha\beta + \gamma\delta$ are determined. There remain two ambiguities: 1) VA $\alpha \leftrightarrow \beta$, $\gamma \leftrightarrow \delta$, and 2) isoscalar - isovector $\alpha \leftrightarrow \gamma$, $\beta \leftrightarrow \delta$, which have to be resolved by other experiments.⁴ More importantly, the establishment that these ratios are constant shows that the x dependence of the neutral current structure functions are the same as the charged current structure functions. This test is free of flux normalization uncertainties.

The antiquark remainder terms can be measured by observing any deviation of the ratios from a constant at small x where the $x\bar{q}$ term is expected to be at its maximum. However if $\sin^2 \theta_w = 0.25$, then $a = 0.297$, $\bar{a} = 0.130$ and $b = 0.320$. Thus $4/3(b-a) = 0.031$ and $4/3 b - 4\bar{a} = 0.093$ and consequently the $x\bar{q}$ term is suppressed offering little sensitivity to the antiquark sea. Thus the ratios should be quite constant.

b) Test 2

By computing the sums and differences of the neutral current and charged current neutrino and antineutrino cross sections, the structure functions $F_2(x, Q^2)$ and $xF_3(x, Q^2)$ may separately be determined for each interaction. Referring to equation 9 and Table I, we have (assuming $R = 0$)⁵

Charged-Currents:

$$\frac{d\sigma^{\nu}}{dx dy} + \frac{d\sigma^{\bar{\nu}}}{dx dy} = \frac{G^2 m E_{\nu}}{\pi} F_2(x, Q^2) (1 + (1 - y)^2) \quad (11a)$$

$$\frac{d\sigma^{\nu}}{dx dy} - \frac{d\sigma^{\bar{\nu}}}{dx dy} = \frac{G^2 m E_{\nu}}{\pi} x F_3(x) (1 - (1 - y)^2) \quad (11b)$$

Neutral Currents:

$$\frac{d\sigma^{\nu}}{dx dy} + \frac{d\sigma^{\bar{\nu}}}{dx dy} = \frac{G^2 m E_{\nu}}{\pi} (\delta_1^2 + \delta_2^2 + \delta_3^2 + \delta_4^2) F_2(x, Q^2) (1 + (1 - y)^2) \quad (12a)$$

$$\frac{d\sigma^{\nu}}{dx dy} - \frac{d\sigma^{\bar{\nu}}}{dx dy} = \frac{G^2 m E_{\nu}}{\pi} (\delta_1^2 + \delta_2^2 - \delta_3^2 - \delta_4^2) x F_3(x, Q^2) (1 - (1 - y)^2) \quad (12b)$$

Since $(\delta_1^2 + \delta_2^2)$ and $(\delta_3^2 + \delta_4^2)$ are computed by Test 1, the structure functions for the neutral currents are completely determined. These tests depend on the relative flux normalization between the neutrino and antineutrino narrow band beam exposures. This relative normalization should be good to $\sim 3\%$, and in fact the measurement errors of this test should be dominated by statistical uncertainties.⁹

We can integrate $d\sigma/dx dy$ over x to formulate another ratio test. By computing $\frac{d\sigma^{(\bar{\nu})}}{dy}_{nc} / \frac{d\sigma^{(\bar{\nu})}}{dy}_{cc}$, we compare the y dependence of the neutral current scattering to that of the charged current scattering. This comparison determines again the coupling constants $(\delta_1^2 + \delta_2^2)$ and $(\delta_3^2 + \delta_4^2)$ as well as the ratio of the

total antiquark momentum fraction to the total quark momentum fraction. However this information can be extracted from Test 1 and 2 above. Hence this y dependence ratio test will only serve as a useful consistency check.

The results of Test 2 directly confront QCD. This analysis will provide a direct test of the Q^2 evolution of the structure functions for both charged current and neutral current interactions.

IV. Design of the Experiment

a) Method

The incident neutrino energy must be known to determine the neutral current kinematics. Thus the data have to be taken in the narrow band beam. The calorimeter will determine the energy and angle of the recoil hadron shower and the recoil muon momentum in the case of the charged current event. This information determines the complete neutral current kinematics (0c fit) and over determines the charged current events. The kinematics for 500 GeV incident neutrino energy - a typical value, is shown in figure 3.

To reduce the uncertainties in the comparison of charged current events with neutral current events, a subclass of charged current events will be analyzed with the same cuts which are applied to the neutral current events. Since the kinematics of this subclass of events is overdetermined by using the muon momentum, an important check of the method of analyzing the neutral currents can be performed.

In the narrow band beam, the energy of the neutrino is fixed by measuring the angle of the neutrino about the K/π momentum direction. The K/π ambiguity for neutral current events is resolved by demanding that the recoil hadron energy of the event be greater than the neutrino energy from $\pi \rightarrow \mu \nu$ decay at that particular angle. This results in a y_{\min} cut at low y . The incident neutrino angle is measured by the radius of vertex of the neutrino interaction and the average distance of the K/π decay point from the neutrino detector.

A Monte Carlo simulation of the energy versus radius of the proposed narrow band beam D-61G is shown in figure 4. This was computed by taking the K/π momentum to be 600 GeV/c and assuming gaussian angular and momentum divergences of $\sigma(\theta) \sim 0.05$ mrad and $\sigma p/p \sim 5\%$ respectively. The corresponding energy resolution versus radius is shown in figure 5.

b) Resolutions:

The kinematic variables of interest are $x = Q^2/2m_p E_h$, $y = E_h/E_\nu$ and $Q^2 = 2E_\nu E_\nu' (1 - \cos\theta_\nu')$ (E_ν' and $\theta_\nu' \rightarrow E_\mu', \theta_\mu'$ respectively for charged current events.) By the small angle approximation:

$$Q^2 \cong E_\nu E_\nu' \theta_\nu'^2 \cong \frac{(E_h \theta_h)^2}{(1-y)}, \text{ thus } x = \frac{E_h \theta_h^2}{2m_p(1-y)}$$

The resulting errors in x are then:

$$\left(\frac{\sigma x}{x}\right)^2 = 4\left(\frac{\sigma \theta}{\theta}\right)^2 + \frac{1}{(1-y)^2} \left(\frac{\sigma E_h}{E_h}\right)^2 + \left(\frac{y}{(1-y)}\right)^2 \left(\frac{\sigma E_\nu}{E_\nu}\right)^2$$

and the corresponding measurement errors in y are:

$$\left(\frac{\sigma y}{y}\right)^2 = \left(\frac{\sigma E_\nu}{E_\nu}\right)^2 + \left(\frac{\sigma E_h}{E_h}\right)^2$$

Only the hadron shower energy and angle are measured in neutral current interactions. Figures 6 and 7 show the hadron energy and shower angle distributions respectively for accepted neutral current events. Approximately 70% of the events have a hadron energy below 200 GeV. Good angular resolution at "low"

energies is important even at the Tevatron. The energy and angle resolutions are discussed in Appendix A.

The resolutions in x , using $\sigma(\theta_h)$ given by figure A6 for various values of y at $E_\nu = 500$ GeV as shown in figure 8. The primary error in σ_x is caused by the uncertainty in θ_h . The resolution in x degrades as y increases. The contribution due to Fermi motion of the target nucleons is estimated to be $\frac{\sigma_x}{x} \approx 15\%$. Hence the uncertainties in x are primarily caused by the uncertainty in θ_h over much of the y region. Estimating $\sigma(E_\nu)/E_\nu \sim 10\%$ and $\sigma(E_h)/E_h \sim \frac{100\%}{\sqrt{E_h}}$ for $E_h > 200$ GeV (proportional tubes pulse height) and $\sigma(E_h)/E_h \sim 7\%$ for $E_h < 200$ GeV (flash chambers cell counting), we obtain the resolution in y given by figure 9.

In section VI we will show by a Monte Carlo simulation that these x and y resolutions are adequate to discern QCD effects in the $Q^2 \lesssim 400$ (GeV/c)² range, and to make a good comparison of the neutral current structure functions with charged current structure functions.

c) Beam Energy:

A K/π momentum of 600 GeV/c is chosen to compromise between high energy (large Q^2), and event rate. The $Q^2 - y$ values for various choices of x are given in figure 10. We see that $Q^2 \lesssim 400$ (GeV/c)² is accessible. In figure 11, we have plotted the hadron mass distribution for neutrino-neutral current events. Masses up to ~ 30 GeV/c² are accessible.

V) Event Rates:

The event rates in the narrow band beam D-61G (L. Stutte)¹⁰ in a 100 fiducial ton (340 Ton total) lab C detector are given in Table II . The K/ π momentum was chosen to be 600 GeV/c at the Tevatron operating at 1000 GeV. The beam exposure was taken at 4.4×10^{18} protons on target for antineutrino running and 1.0×10^{18} protons on target for neutrino running. This corresponds to one year of beam at the "standard" Tevatron delivering 10^{13} protons on target each 60 seconds. Both the neutral current and the charged current event rates include the y_{\min} cut to separate neutrinos for K decay from neutrinos from π decay. No y_{\min} cut has been applied to the π decay events.

Table II

		K	π	Total
Neutral Current	ν	5000	3960	8960
	$\bar{\nu}$	1000	4920	5920
charged current	ν	16700	12000	28700
	$\bar{\nu}$	2900	14500	17420

grand total 61,000

With this beam exposure, the number of events per 12 GeV^2 bin in Q^2 is shown in figure 12. Thus, the measurable Q^2 range extends to $Q^2 \sim 400 (\text{GeV}/c)^2$.

VI) Monte Carlo Simulation

a) Method

In this section we describe the results of a monte carlo simulation of the neutral current and the charged current deep inelastic scattering in the narrow band beam. The object is to generate events with QCD effects, experimental uncertainties, and the statistics imposed by the event rates of Table II.

The elements of the simulation are:

- 1) The narrow band beam D-61G with $P_{K/\pi} = 600 \text{ GeV/c}$, $\sigma(\theta) = 0.05 \text{ mrad}$, $\sigma/p \sim 5\%$. (See figures 4 and 5).
- 2) The experimental uncertainties of the hadron energy and angle determination given by figures 4 and 6 of Appendix A.
- 3) The shower containment requiring 99% longitudinal and 95% lateral (see figure 3 Appendix A) containment.
- 4) The neutrino-nucleon cross sections given by equations 4 through 7, but neglecting the strange and charm sea. $\sin^2 \theta_w = 0.25$.
- 5) The QCD effects are put into $F_2(x, Q^2)$ and $xF_3(x, Q^2)$ using the parameterization of Buras and Gaemers.¹¹ $R = F_L(x, Q^2)/F_2(x, Q^2)$ is taken to be 0.
- 6) The statistics imposed by 5000 neutrino events and 1000 antineutrino events.

The simulated data are analyzed to extract a cross section $\frac{d\sigma}{dx dy}$ corrected for experimental effects as follows:

$$\frac{d\sigma}{dx dy} = \frac{\frac{dN}{dx dy}}{\frac{dM}{dx dy}} \left(\frac{d\sigma}{dx dy} \text{ theory} \right)$$

where $\frac{dN}{dx dy}$ = accepted Monte Carlo events with QCD effects, experimental measurement uncertainties, and shower containment; $\frac{dM}{dx dy}$ = accepted Monte Carlo events without QCD, but everything else mentioned above, and $\frac{d\sigma}{dx dy} \text{ theory}$ = monte carlo generating function (x and y distributions) of $\frac{dM}{dx dy}$. The "measurement" should be roughly independent of the choice of $\frac{dM}{dx dy}$ and its generator $\frac{d\sigma}{dx dy} \text{ theory}$.

b) Results

The results of Test 1, where we compute the ratio of neutral current cross sections to charged current cross sections for both neutrino and antineutrino interactions, are shown in figures 13a and 13b. From this ratio test, we determine the value of $(\delta_1^2 + \delta_2^2) = 0.29 \pm 0.01$ and $(\delta_3^2 + \delta_4^2) = 0.035 \pm 0.008$, and finally we retrieve $\sin^2 \theta_w = 0.25 \pm 0.01$.

The extraction of the structure functions F_2 and xF_3 in Test 2 is accomplished by taking the sum and differences of the neutrino and anti-neutrino cross sections and is therefore subject to the neutrino flux normalization errors. These errors have been estimated to be $\sim 3\%$.⁹ The results of this test are shown in figure 14 for the neutral current interactions and in figure 15 for the charged current interactions. The lines through the data are the input functions with QCD effects according to Buras and Gaemers.

To see the Q^2 evolution of the structure functions more directly, we plot $F_2(x, Q^2)$ for a given constant value of x versus Q^2 . These are shown in figures 16 and 17 for neutral currents and charged currents respectively. The lines through the data are the input functions of Buras and Gaemers. The data follow the input functions quite closely, showing that the measurement of the structure functions is limited by statistical and not systematic errors due to resolution smearing effects. From these graphs it is evident that most of the Q^2 dependence is in the region $Q^2 < 50 \text{ (GeV/c)}^2$. Above $Q^2 \sim 100 \text{ (GeV/c)}^2$, $F_2(x, Q^2)$ for constant x is almost flat.

Since the QCD effects are logarithmic, the variation with Q^2 of $F_2(x, Q^2)$ for Q^2 between 50 (GeV/c)^2 and 400 (GeV/c)^2 is typically less than $\sim 20\%$. Hence, in the high Q^2 region, scaling should again be approximately true. Any deviation from the predictions of QCD should be quite striking. In fact, boson propagator effect should be $\sim 10\%$ for $Q^2 \sim 400 \text{ (GeV/c)}^2$ and should eventually dominate the QCD effects at high Q^2 .

Finally, to make the comparison between neutral current structure functions and the charged current structure functions more explicit, we plot the ratios of the two. This is shown in figures 18 and 19. Hence, detailed comparisons of the two interactions will be possible, and in particular the smallness of the term $x\Delta^N(x)$ (see Table I) can be measured.

Multi-lepton Events and New Phenomena

Some hints that there may be interesting new phenomena lurking at higher energies is given by the observation at Fermilab of some extraordinary events that do not readily fit into the accepted mold. These "super" events have visible energy greater than 100 GeV and are characterized by extremely high muon energies. If these events do in fact represent a new interaction seen at Fermilab and not at CERN because of the somewhat harder neutrino spectrum, then the Tevatron neutrino beam could be an extremely copious source of these events. Any attempt at estimating the rates are highly conjectural but if we assume a phase space type excitation with a threshold of 10 GeV then we might expect several hundred such events in our detector in a year's time.

We emphasize that our detector has excellent angular resolution ($\sim 1\text{mr}$) and good P_{\perp} resolution of the hadrons ($\sim 0.5 - 1.0 \text{ GeV}/c$) permitting detailed analysis of these new events that could lead to an understanding of their origin.

VII) Requests

To achieve adequate momentum resolution at Tevatron energies, we require drift chambers between the toroids as described in Appendix A. We require \sim one year of narrow band beam at $\sim 10^{13}$ protons/spill, 1 spill/minute, (5.4×10^{18} protons on target) on the narrow band beam train.

VIII) Conclusions:

We can measure the nucleon structure function for both charged currents and neutral currents to very high Q^2 and thereby test QCD. In addition, we will test the Weinberg-Salam Theory in a new energy range. The very fine granularity of the detector will allow many details of the high energy neutrino interactions to become visible.

Footnotes and References

- 1) J. Ellis; "Status of Perturbative QCD", Photon-Lepton Conf. Fermilab (1979).
- 2) R.M. Barnett; "Testing QCD with Structure Functions at Tevatron Energies", Fermilab Tevatron Muon-Neutrino Workshop (1980).
- 3) A.J. Buras; Fermilab - Pub - 79/17-thy
- 4) J.J. Sakurai; International School of Subnuclear Physics, Erice, Sicily (1976).
- 5) In the Monte Carlo calculations of this proposal, we have assumed that $R = F_L(x, Q^2)/F_2(x, Q^2) = 0$. However, there are good theoretical reasons and some experimental data to believe that this assumption is not true. In fact, the Q^2 evolution of $F_L(x, Q^2)$ depends critically on the gluon density. This in turn depends on the gluon self coupling (figure 2c), which is a crucial element of the Yang - Mills structure of QCD. Hence there is a strong motivation for attempting the difficult measurement of this quantity. (See E. Reya; DESY 79/15, and G. Altarelli and G. Martinelli; Phys. Lett. 76B, 89(1978)).

In principle, R may be determined by measuring:

$$\frac{d\sigma^{\nu}}{dx dy} + \frac{d\sigma^{\bar{\nu}}}{dx dy} = \frac{G^2 m E_{\nu}}{\pi} F_2(x, Q^2) [1 + (1-y)^2 - R y^2]$$

at a fixed x and Q^2 , while varying y. Thus, the incident neutrino energy must be varied while holding E_h constant. This procedure is aided by the wide range of energies in the Tevatron narrow band beam.

By the equation above, the extraction of $F_2(x, Q^2)$ depends on R. But $x F_3(x, Q^2)$ does not, since it is determined by the differences of cross sections. Altarelli and Martinelli estimate that R will be large at small x and Q^2 , and will become smaller as both Q^2 and x increase. For $Q^2 \sim 100(\text{GeV}/c)^2$, $R \lesssim 0.1$, thus at $y = 0.9$, R being non zero contributes less than a 8% effect to the extraction of $F_2(x, Q^2)$. At $Q^2 \sim 2(\text{GeV}/c)^2$ and $y \sim 0.9$, the effect of R will be $\lesssim 24\%$ and should be measurable at least for the charged current data.

- 6) E. Reya; DESY 79/30.
- 7) C. Baltay, et al., Phys. Rev. Lett 44, 916(1980)
- 8) U. Amaldi; "Advances in Semileptonic Currents", Neutrino-79 Bergen, Norway (1979).

K. Winter; "Review of Experimental Measurements of Neutral Current Weak Interactions", Photon-Lepton Conf. Fermilab (1979).

- 9) M. Shaevitz; "E-616 - Lab E Neutrino Detector Present Capabilities and Future Plans", Fermilab Tevatron Muon-Neutrino Workshop (1980).
- 10) L. Stutte; TM-841 (1979).
- 11) A.J. Buras and K.J.F. Gaemers; Nuc. Phy. B132, 249(1978).

Figure Captions

- Figure 1a: The charged current interaction: flavor changing
- Figure 1b: The neutral current interaction: flavor diagonal
- Figure 2a: gluon radiation by bremsstrahlung
- Figure 2b: quark-antiquark pair production
- Figure 2c: gluon triple vertex
- Figure 3: Neutral current kinematics for a typical neutrino energy.
- Figure 4: The energy versus radius for neutrinos from K and from π decay. $P_{K/\pi} = 600 \text{ GeV}/c$
- Figure 5: The neutrino energy resolution for the proposed D61G beam with $\frac{\sigma_P}{P} \sim 5\%$ and $\sigma(\theta) \sim 0.05 \text{ mrad}$.
- Figure 6: The expected hadron energy distribution of neutral current events in the neutrino narrow band beam.
- Figure 7: The expected polar angle distribution.
- Figure 8: The resolution in $x = Q^2/2m_p E_h$ as a function of x for various values of y . The resolutions in θ_h , E_h are given in Appendix A. $E_\nu = 500 \text{ GeV}$.
- Figure 9: The resolution in $y = E_h/E_\nu$ as a function of y .
- Figure 10: Q^2 versus y for various values of x for $E_\nu = 500 \text{ GeV}$. Q^2 values up to $400 (\text{GeV}/c)^2$ are accessible. Cuts in a given Q^2 range limit the x range, e.g. low x are inaccessible at large Q^2 .

- Figure 11: The hadron mass distribution for $p_{K/\pi} = 600 \text{ GeV}/c$ narrow band beam neutrino events.
- Figure 12: The experimental Q^2 distribution for neutrino and antineutrino exposures.
- Figure 13a: The results of Test 1: The ratio of neutral currents to charged currents for neutrinos.
- Figure 13b: The result of Test 1 for antineutrinos.
- Figure 14a: The reconstructed neutral current structure functions for $2 \leq Q^2 \leq 40 \text{ (GeV/c)}^2$. The solid line is the input function for $F_2(x, Q^2)$ and the dotted line in the input function of $xF_3(x, Q^2)$ from Buras and Gaemers.
- Figure 14b: $40 \leq Q^2 \leq 80 \text{ (GeV/c)}^2$
- Figure 14c: $80 \leq Q^2 \leq 180 \text{ (GeV/c)}^2$
- Figure 14d: $180 \leq Q^2 \leq 500 \text{ (GeV/c)}^2$
- Figure 15a: The corresponding structure functions for the charged current events analyzed in the same manner, with the same cuts as the neutral current events. $2 \leq Q^2 \leq 40 \text{ (GeV/c)}^2$
- Figure 15b: $40 \leq Q^2 \leq 80 \text{ (GeV/c)}^2$
- Figure 15c: $80 \leq Q^2 \leq 180 \text{ (GeV/c)}^2$
- Figure 15d: $180 \leq Q^2 \leq 500 \text{ (GeV/c)}^2$
- Figure 16: $F_2(x, Q^2)$ for neutral current events for a constant x versus Q^2 . The lines through the data are the QCD input functions of Buras and Gaemers.

Figure 17: $F_2(x, Q^2)$ versus Q^2 for constant x for charged currents.

Figure 18: The ratio of F_2 - neutral current to F_2 - charged currents for given Q^2 bins

Figure 19: The ratio xF_3 - neutral current to xF_3 charged currents for given Q^2 bins

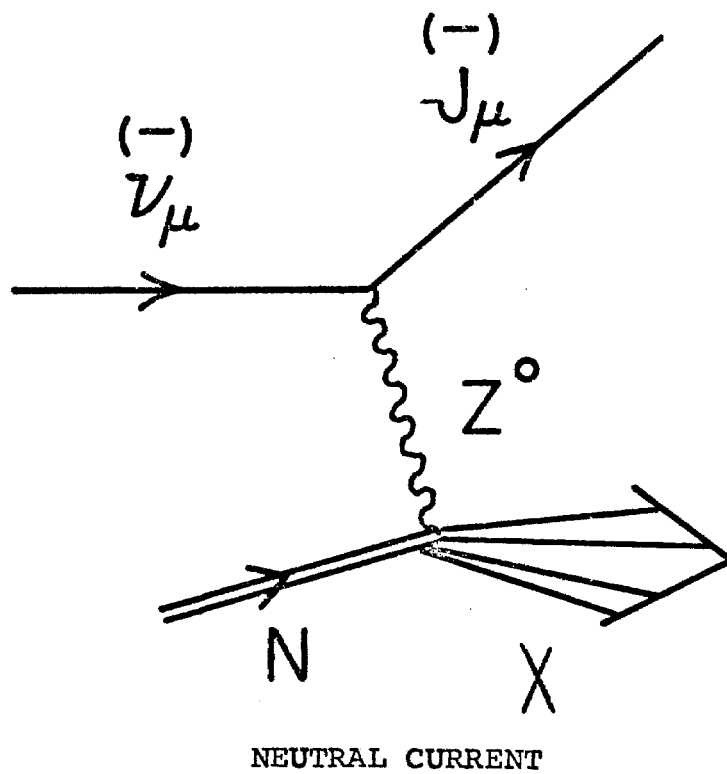
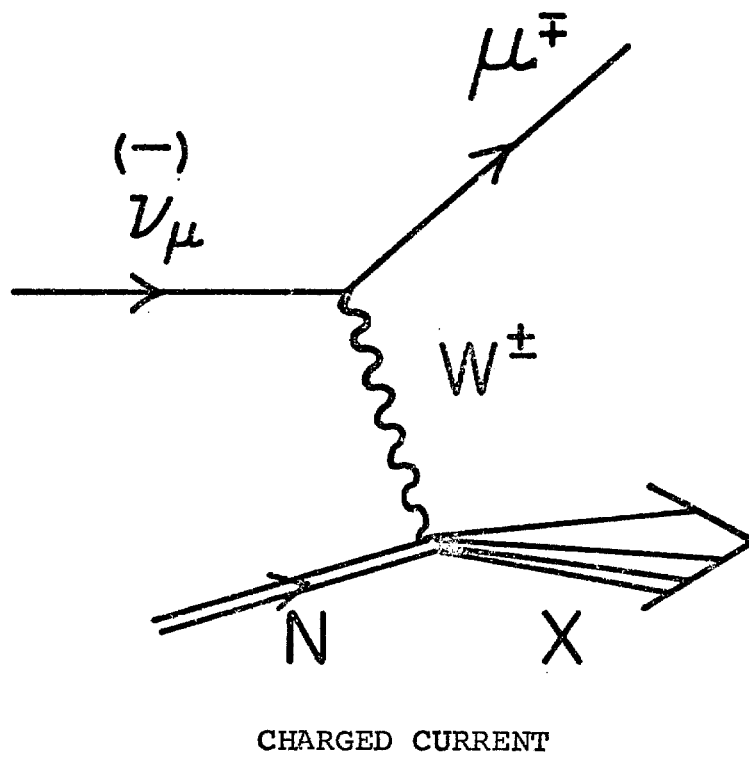


Figure 1

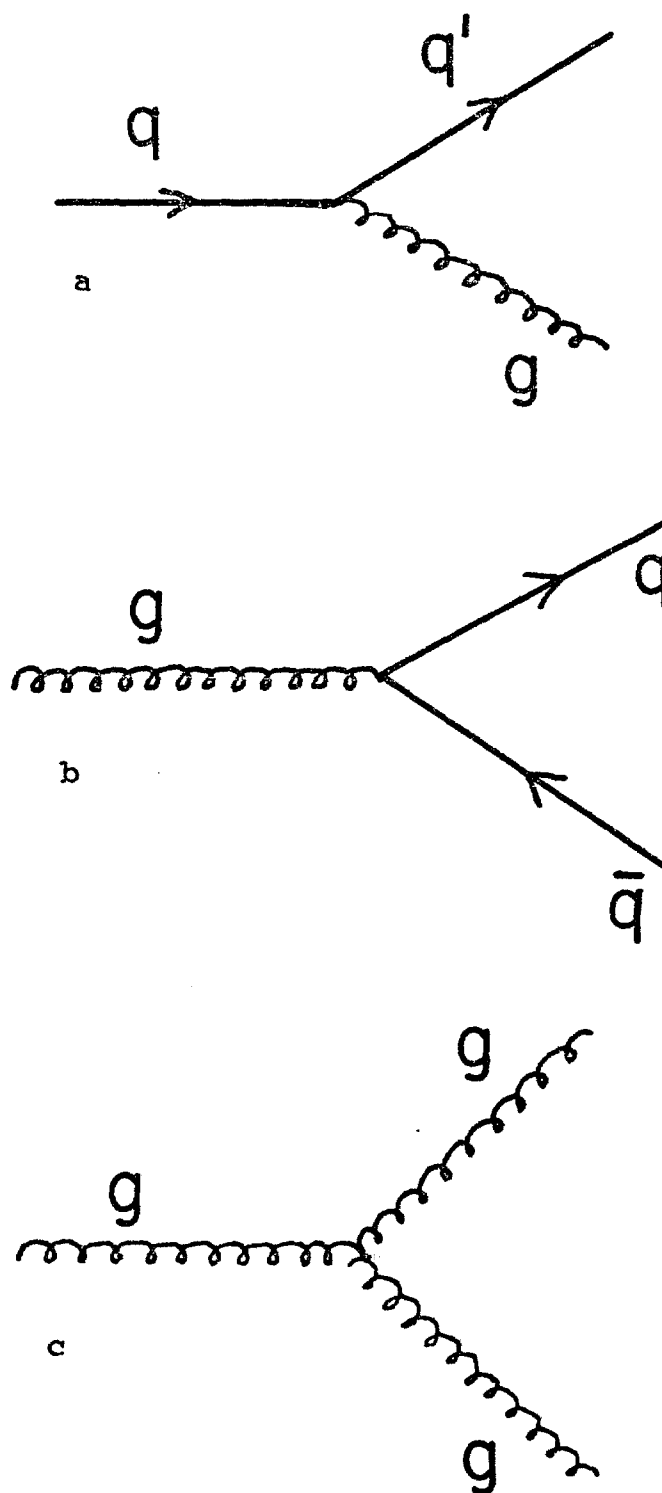


Figure 2

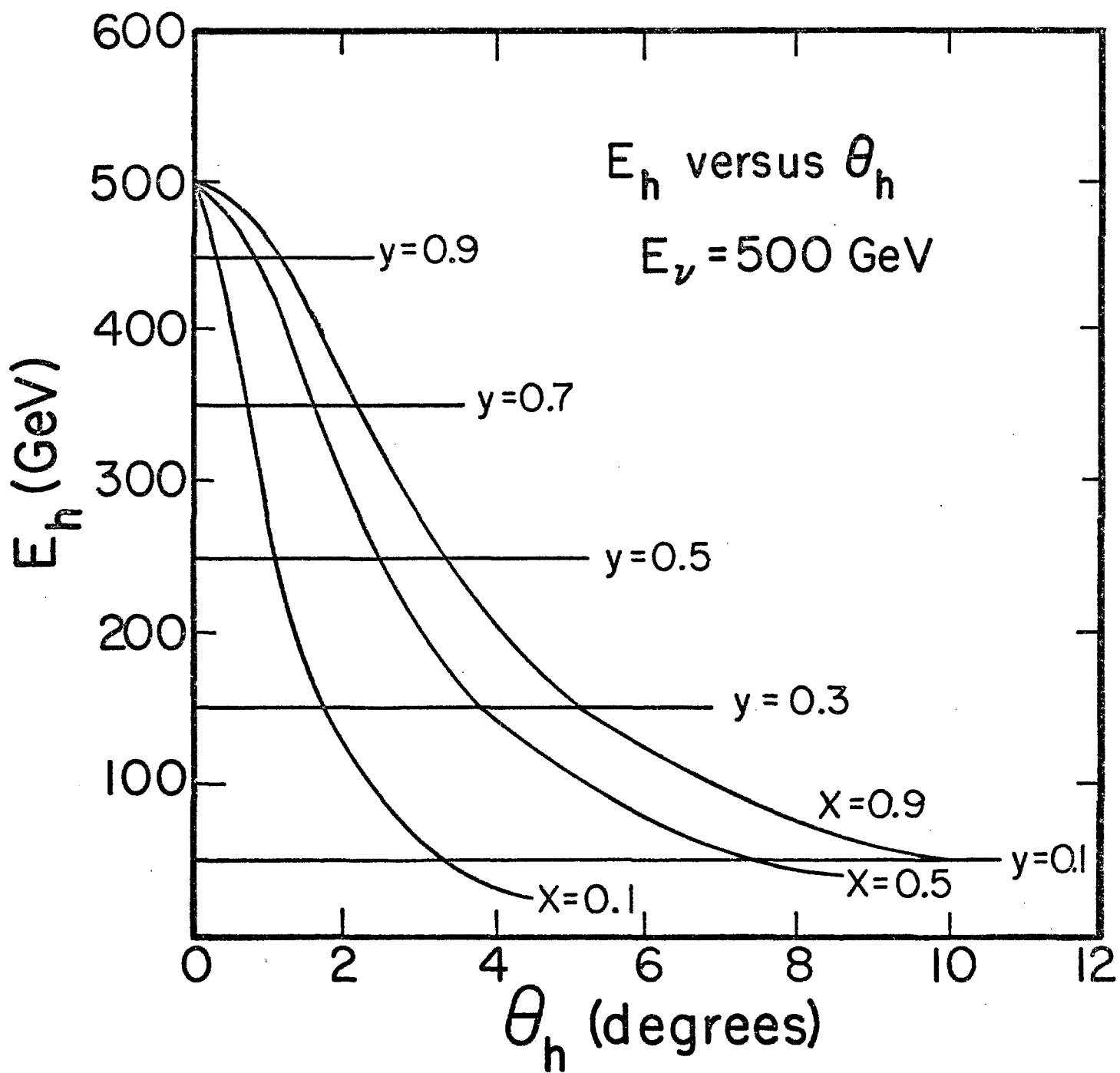


Figure 3

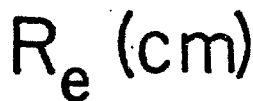
$$P_0 = 600 \text{ GeV/c}$$


Figure 4

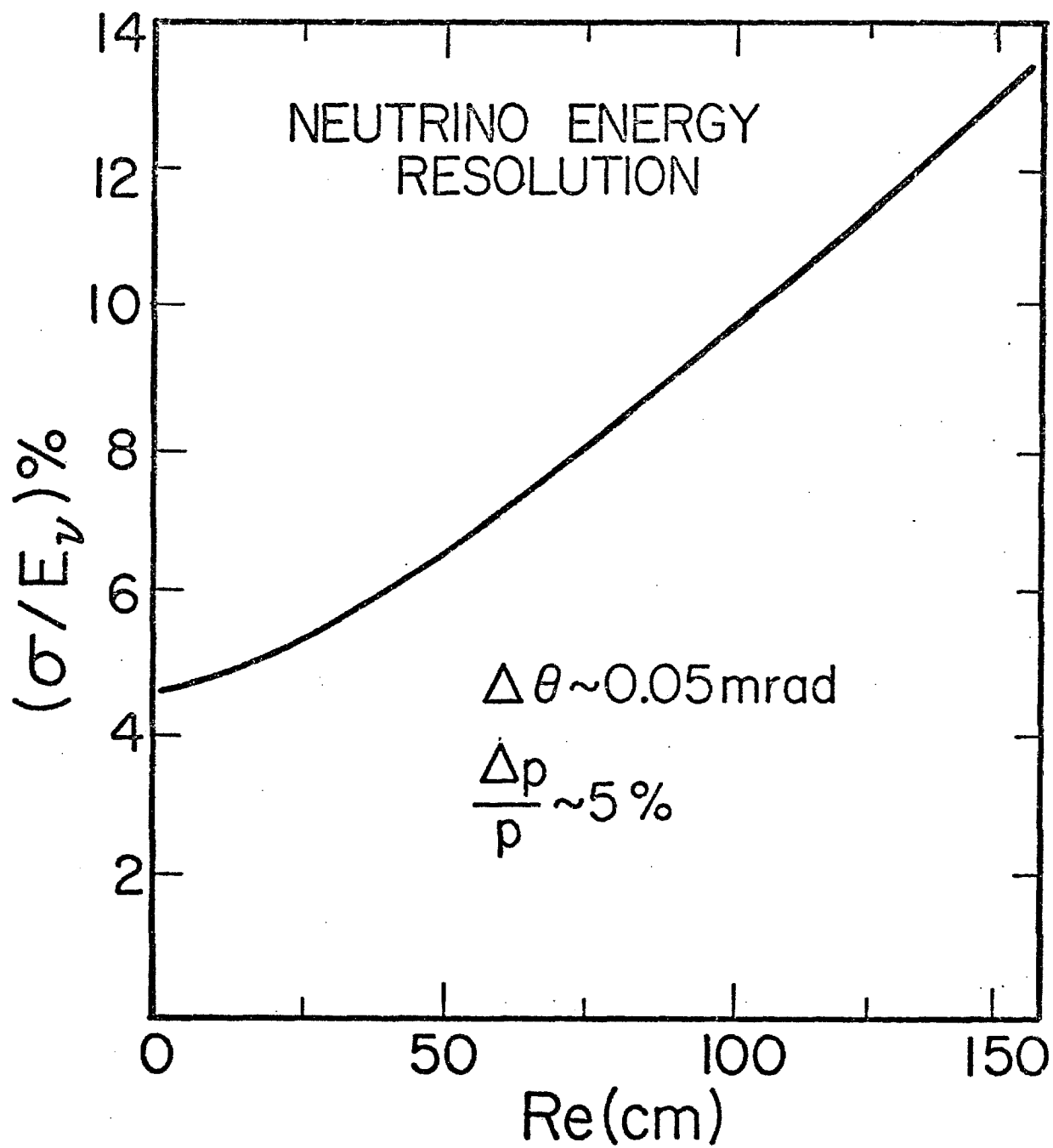


Figure 5

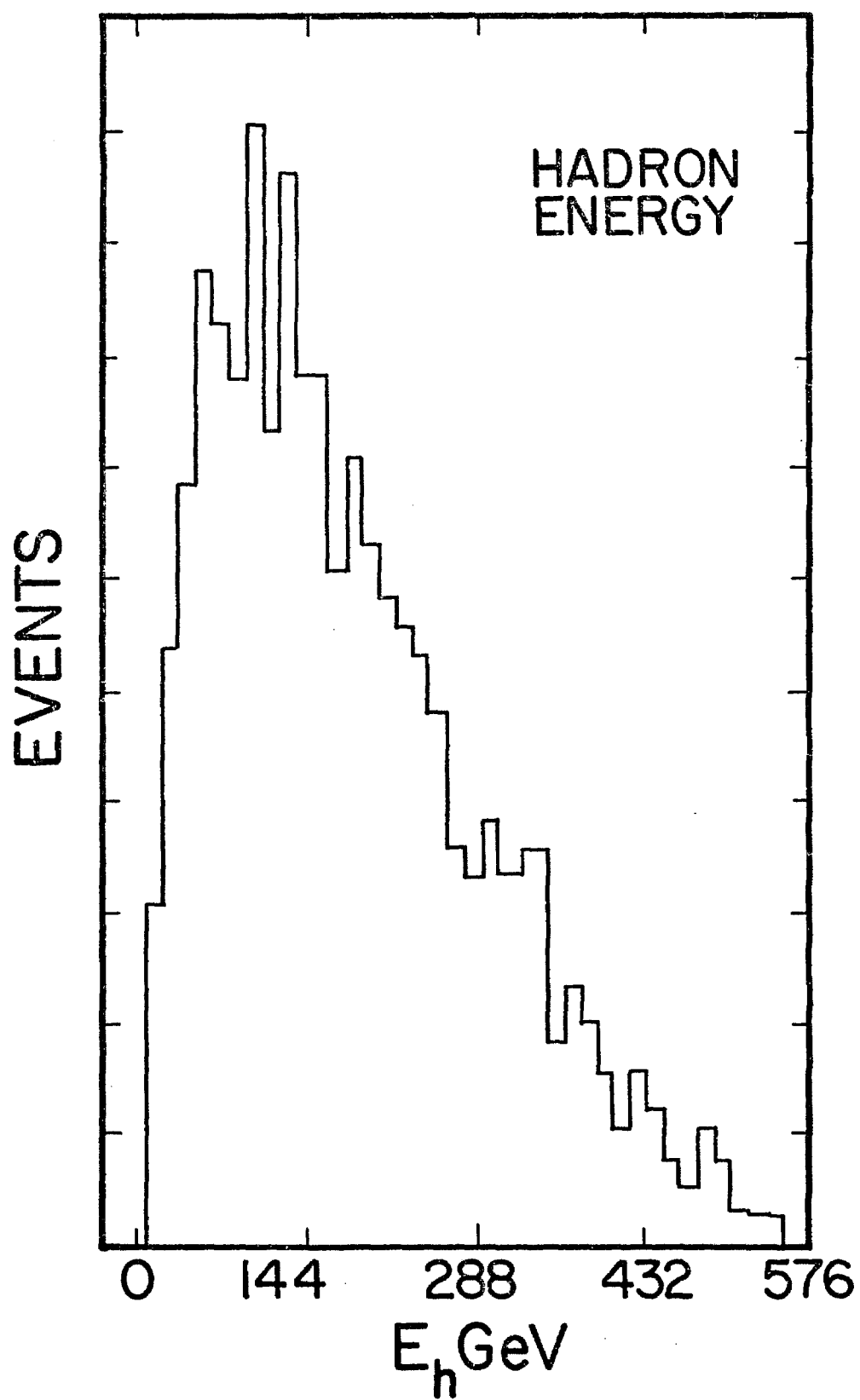


Figure 6

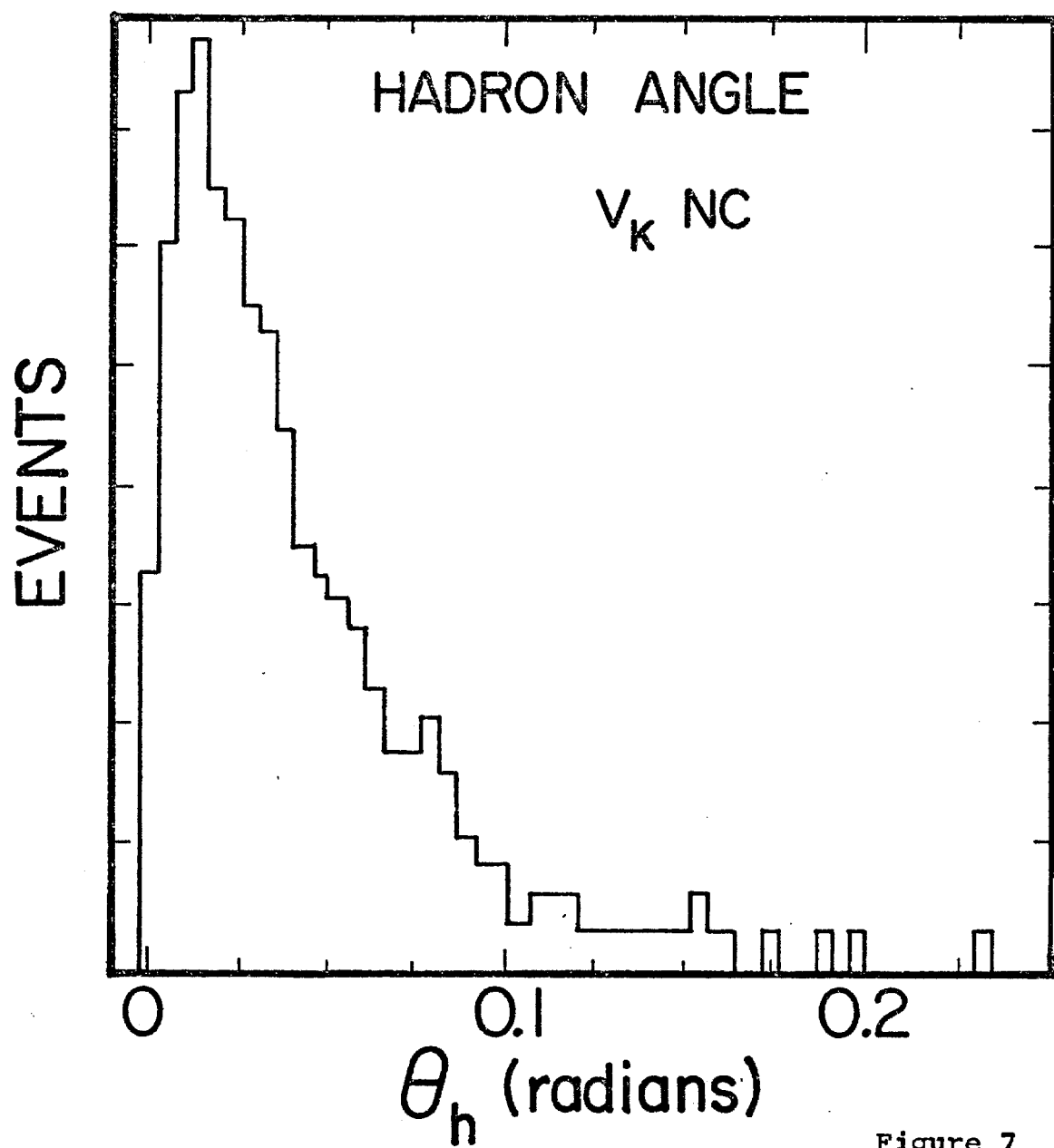


Figure 7

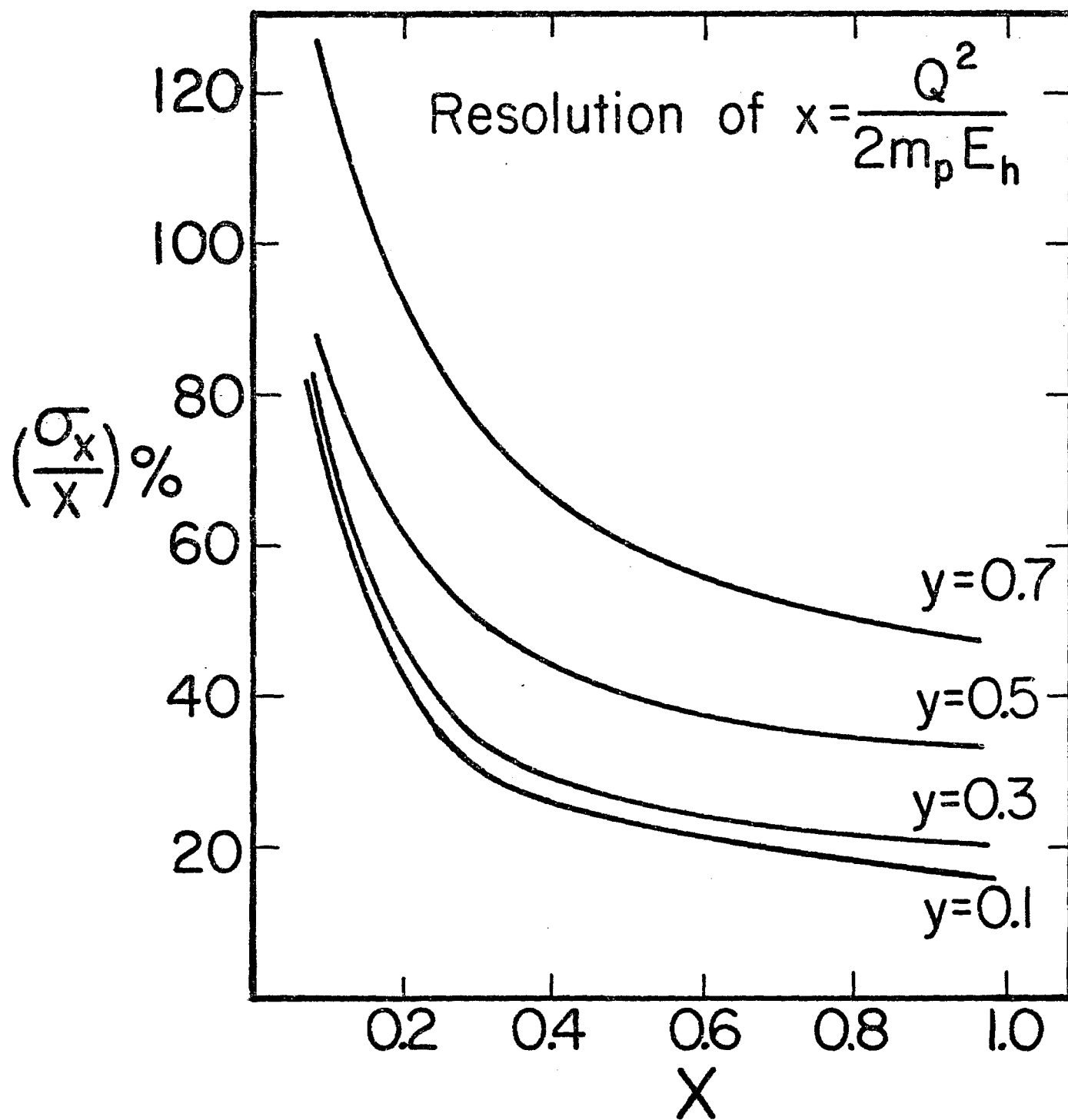


Figure 8

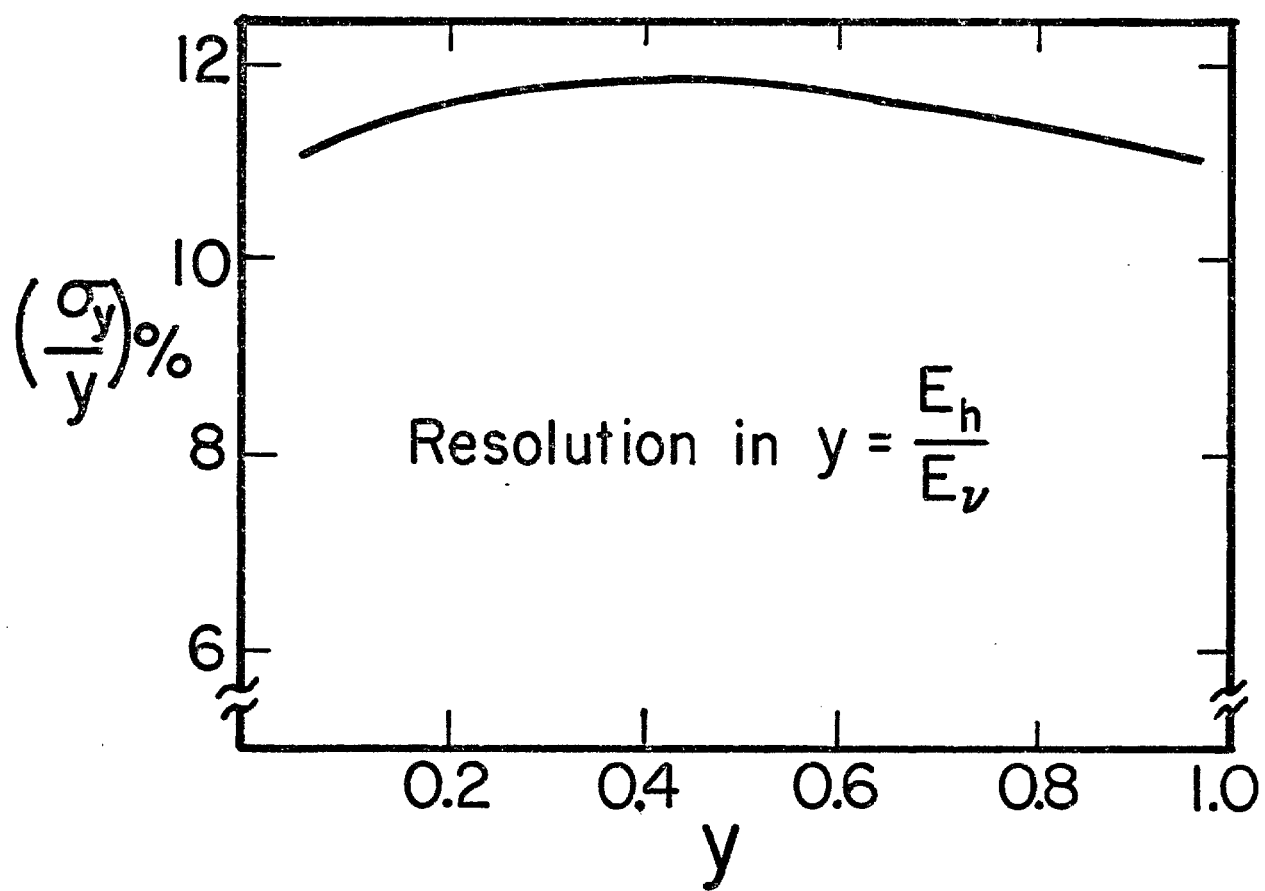


Figure 9

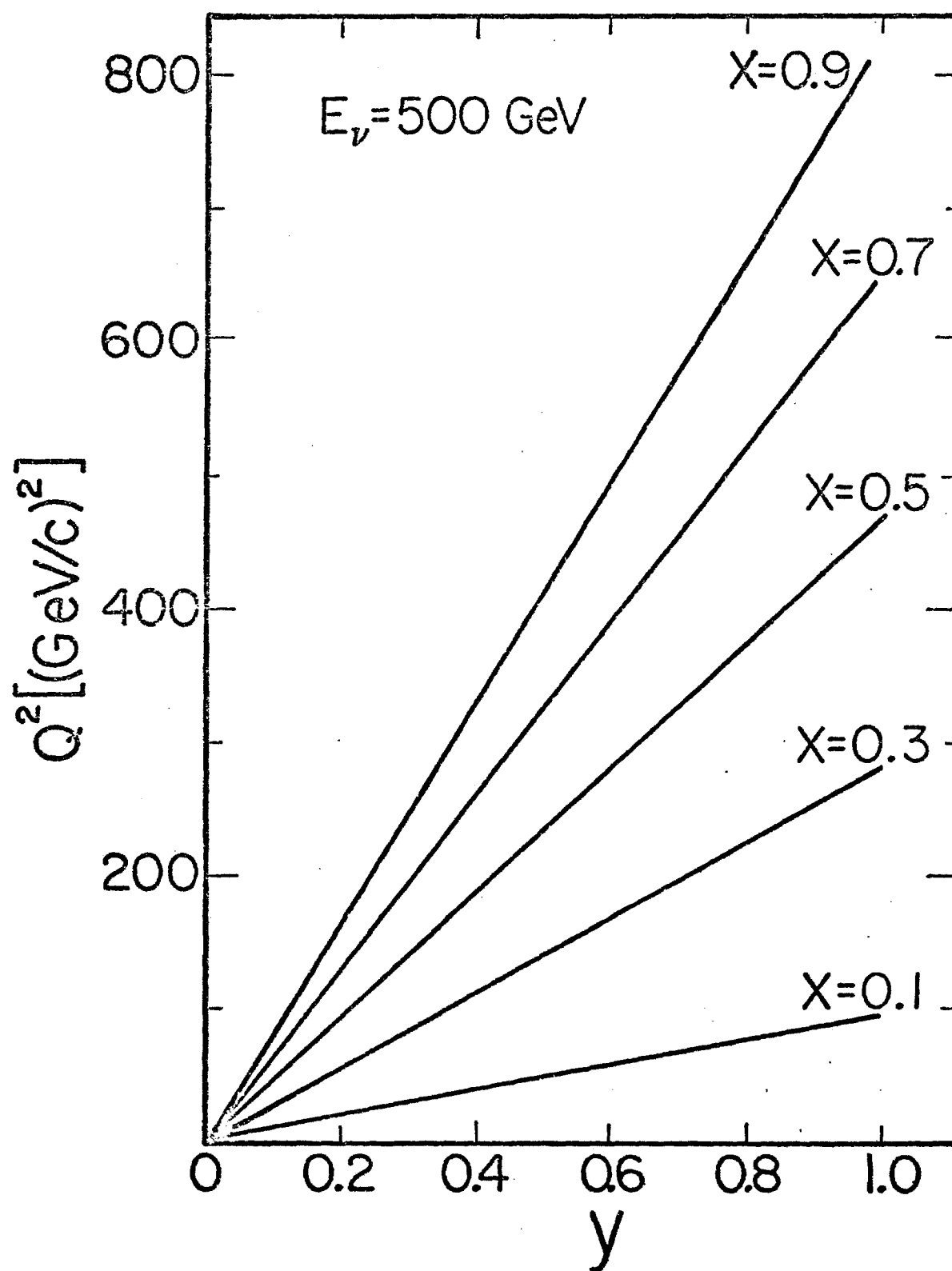


Figure 10

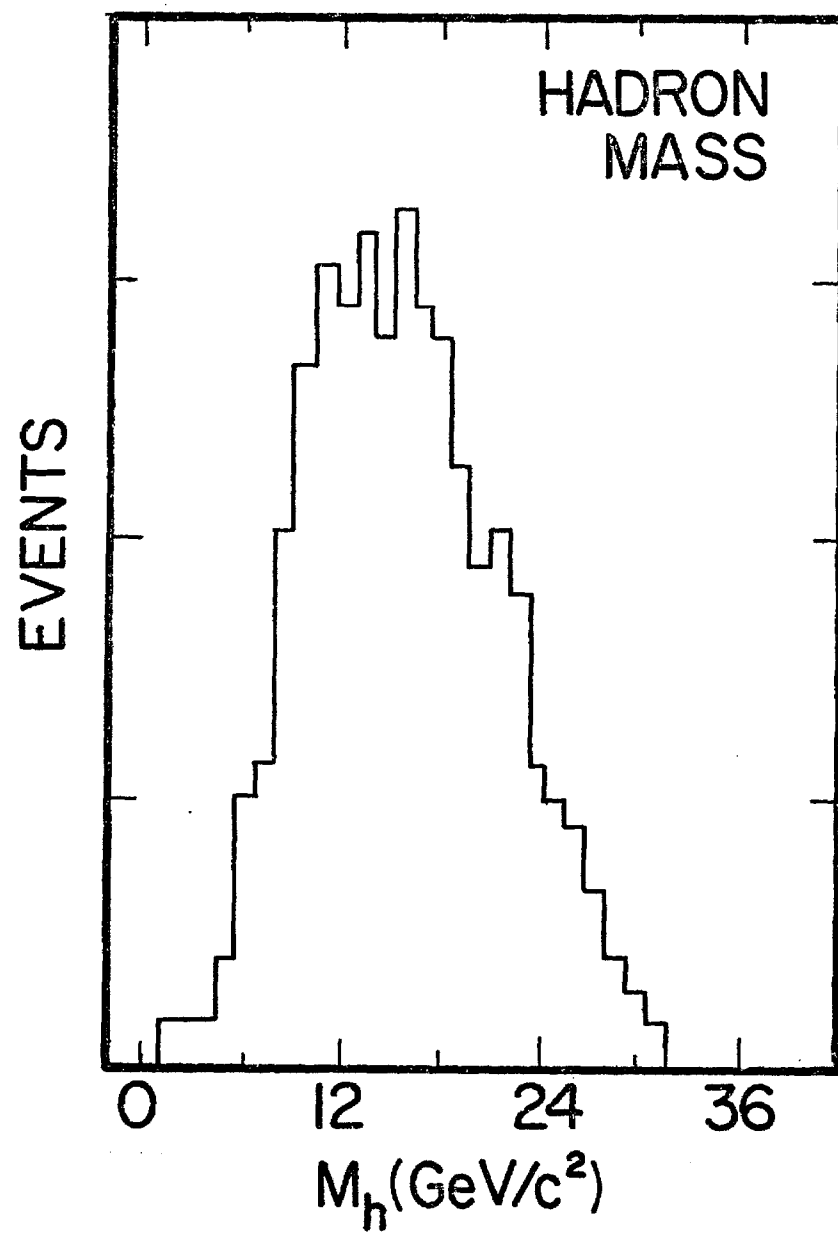


Figure 11

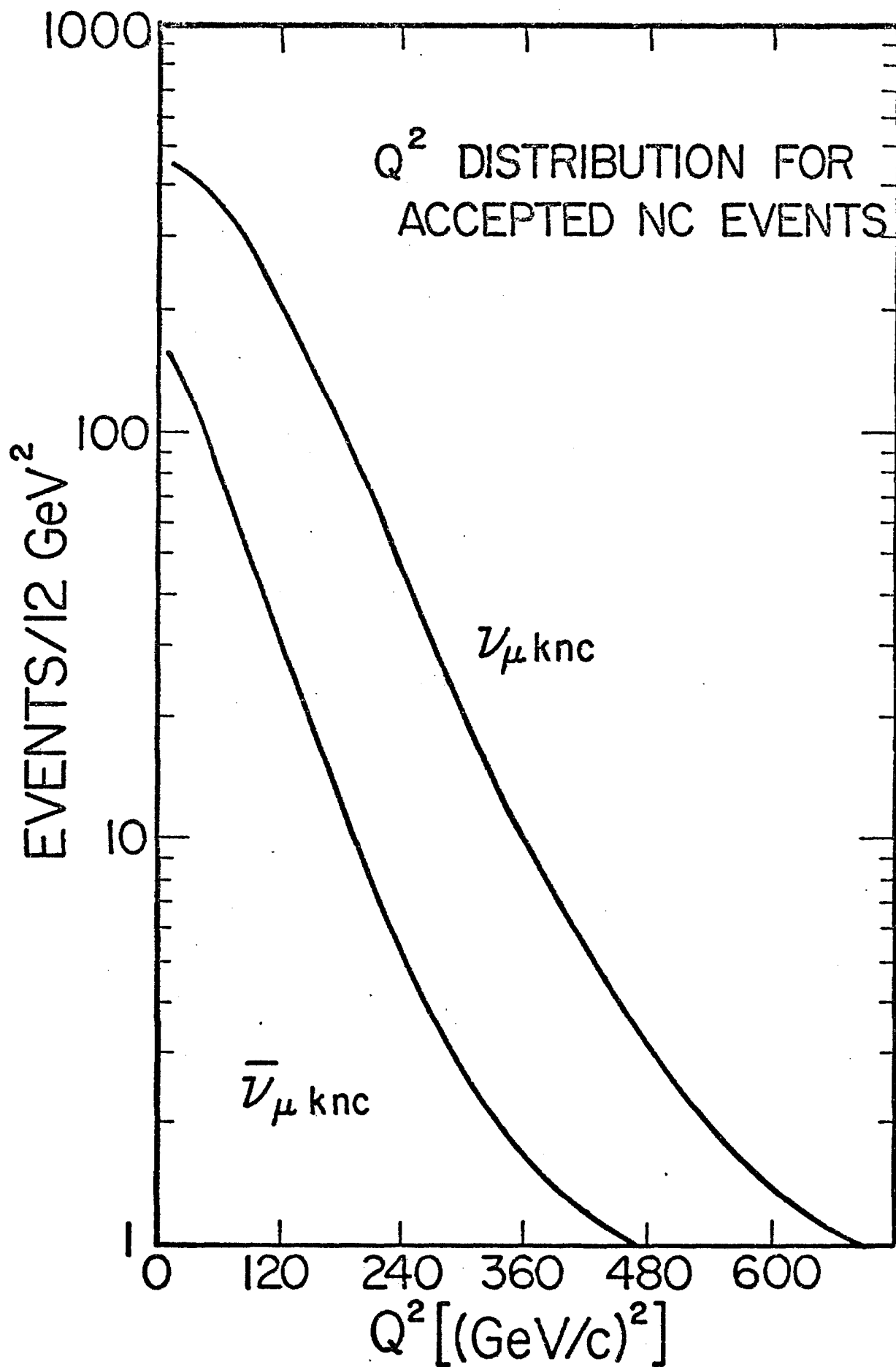


Figure 12

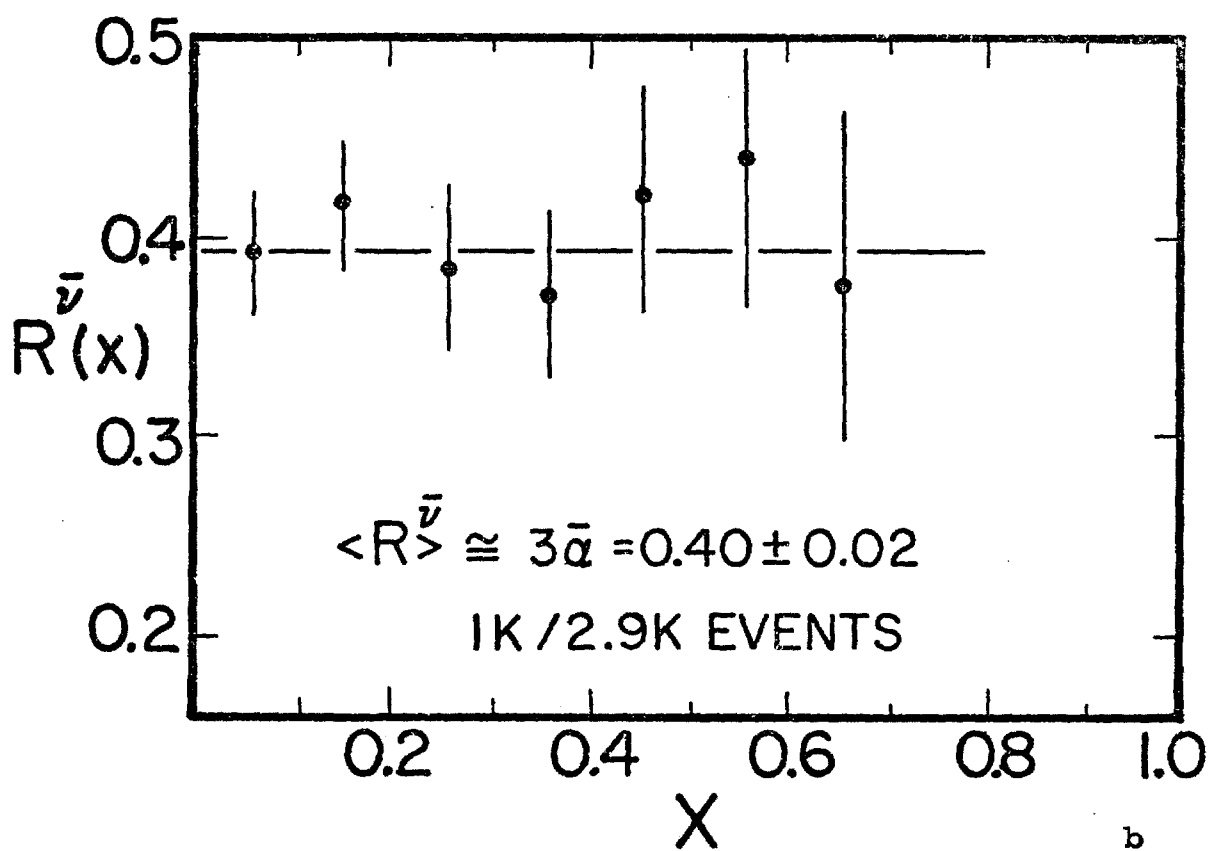
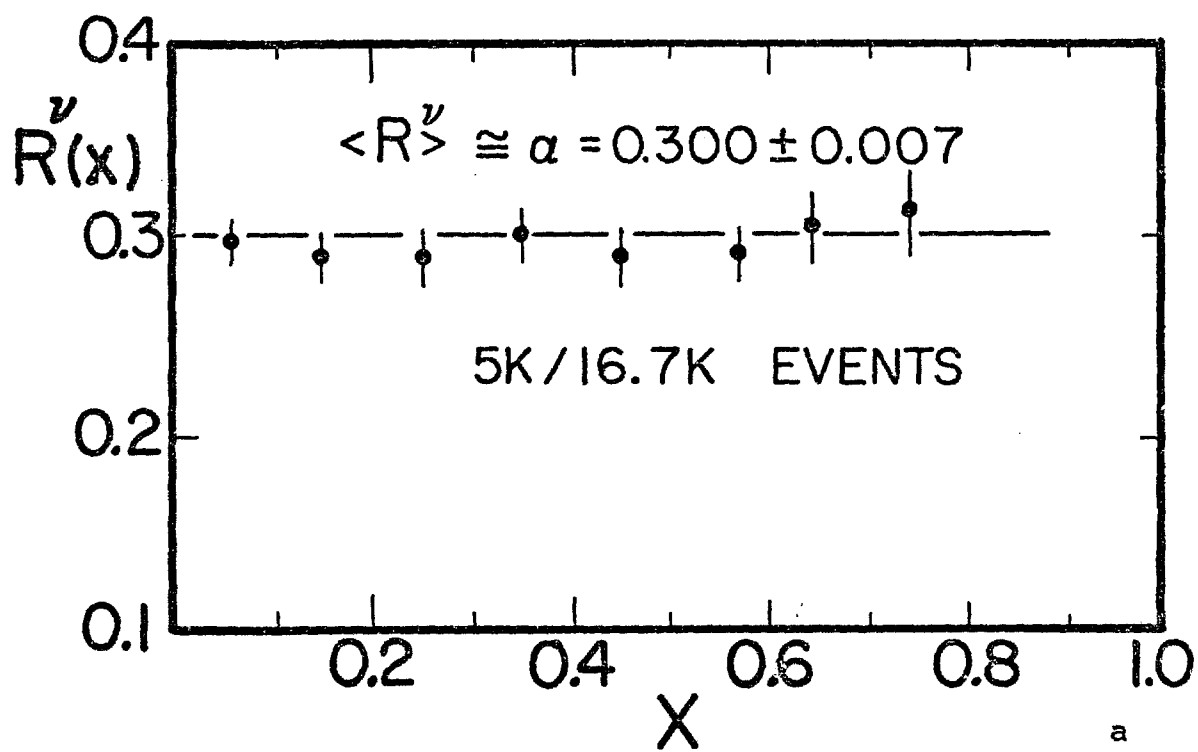


Figure 13

NEUTRAL CURRENTS

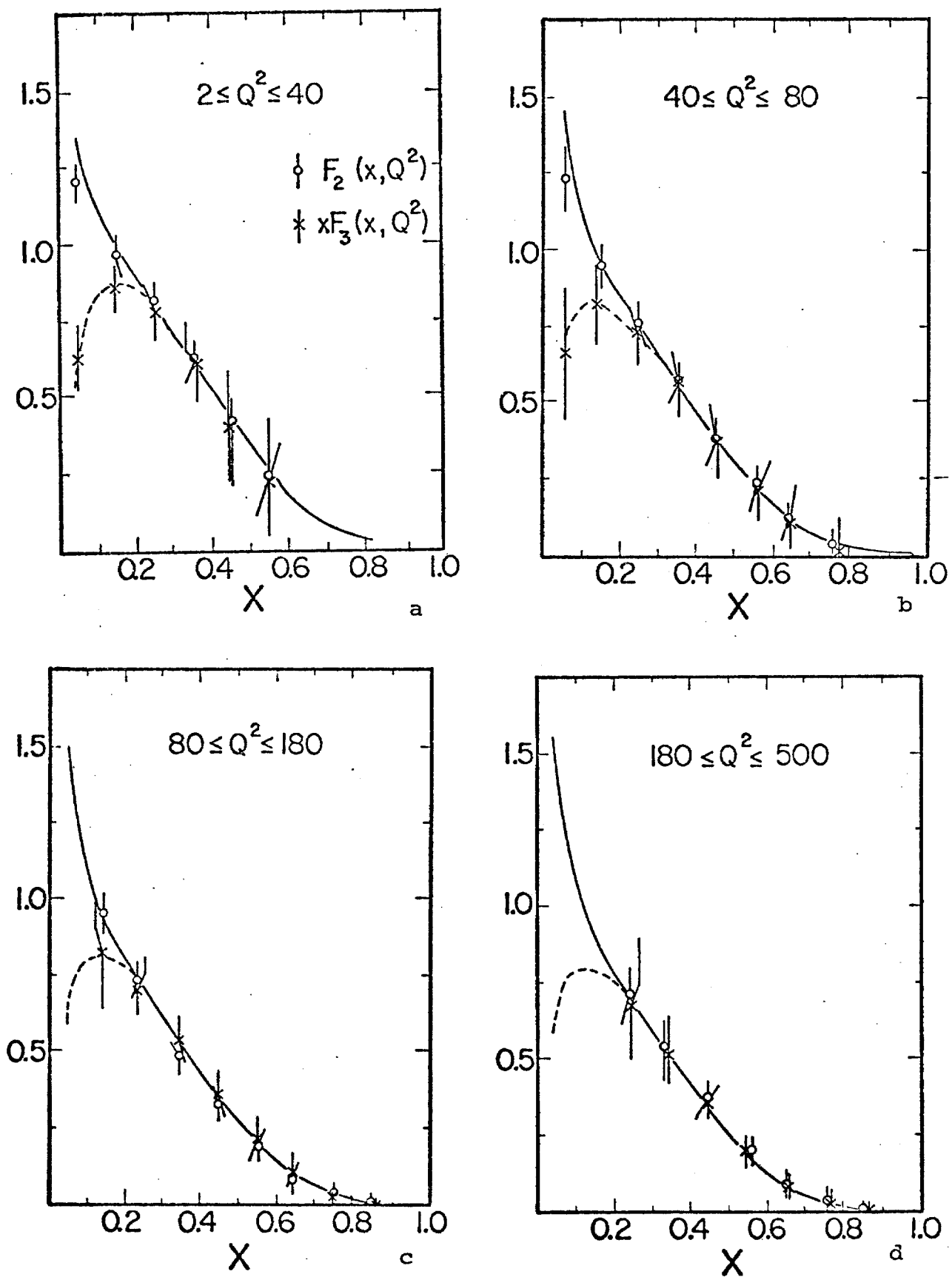


Figure 14

CHARGED CURRENTS

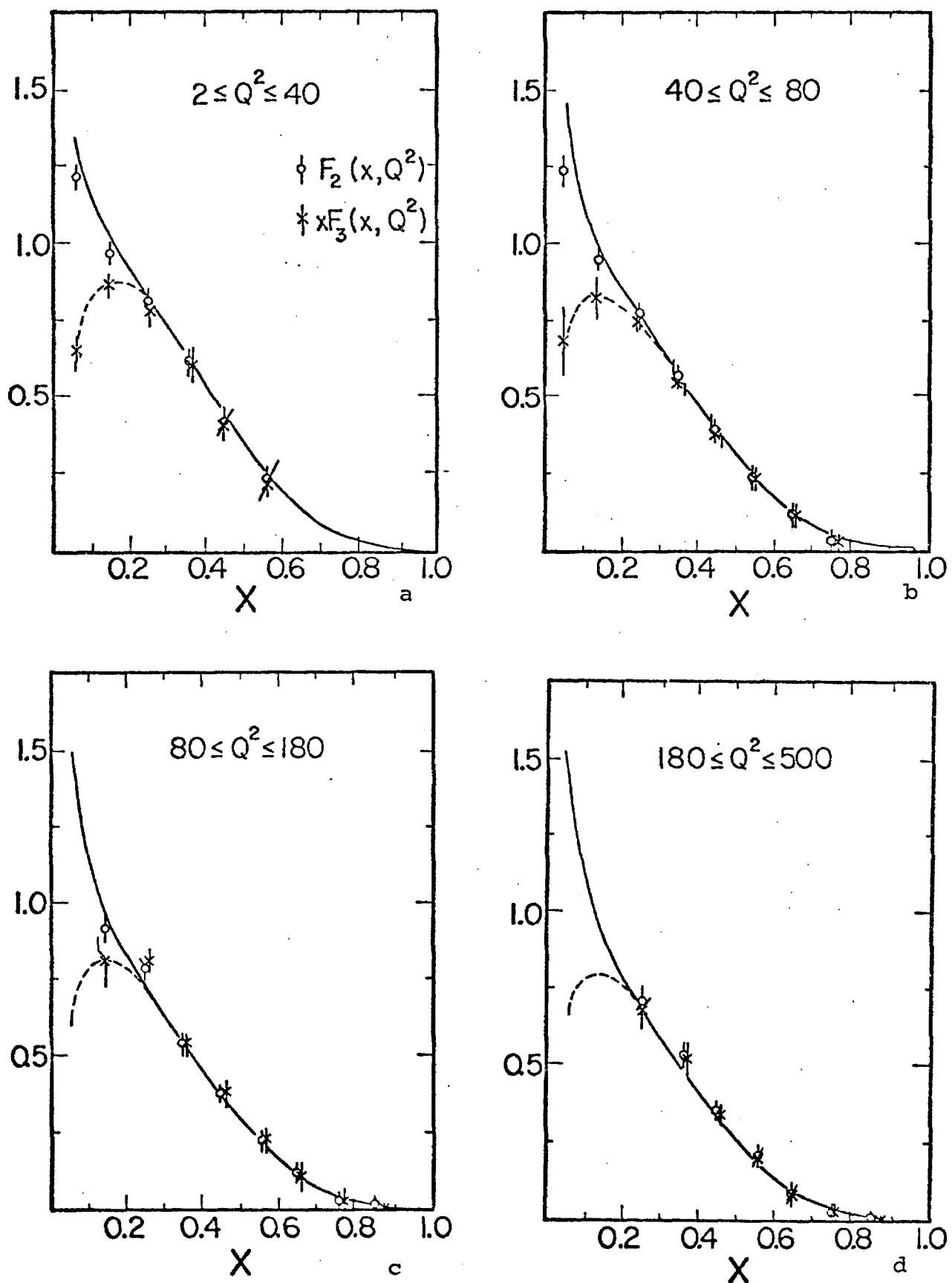


Figure 15

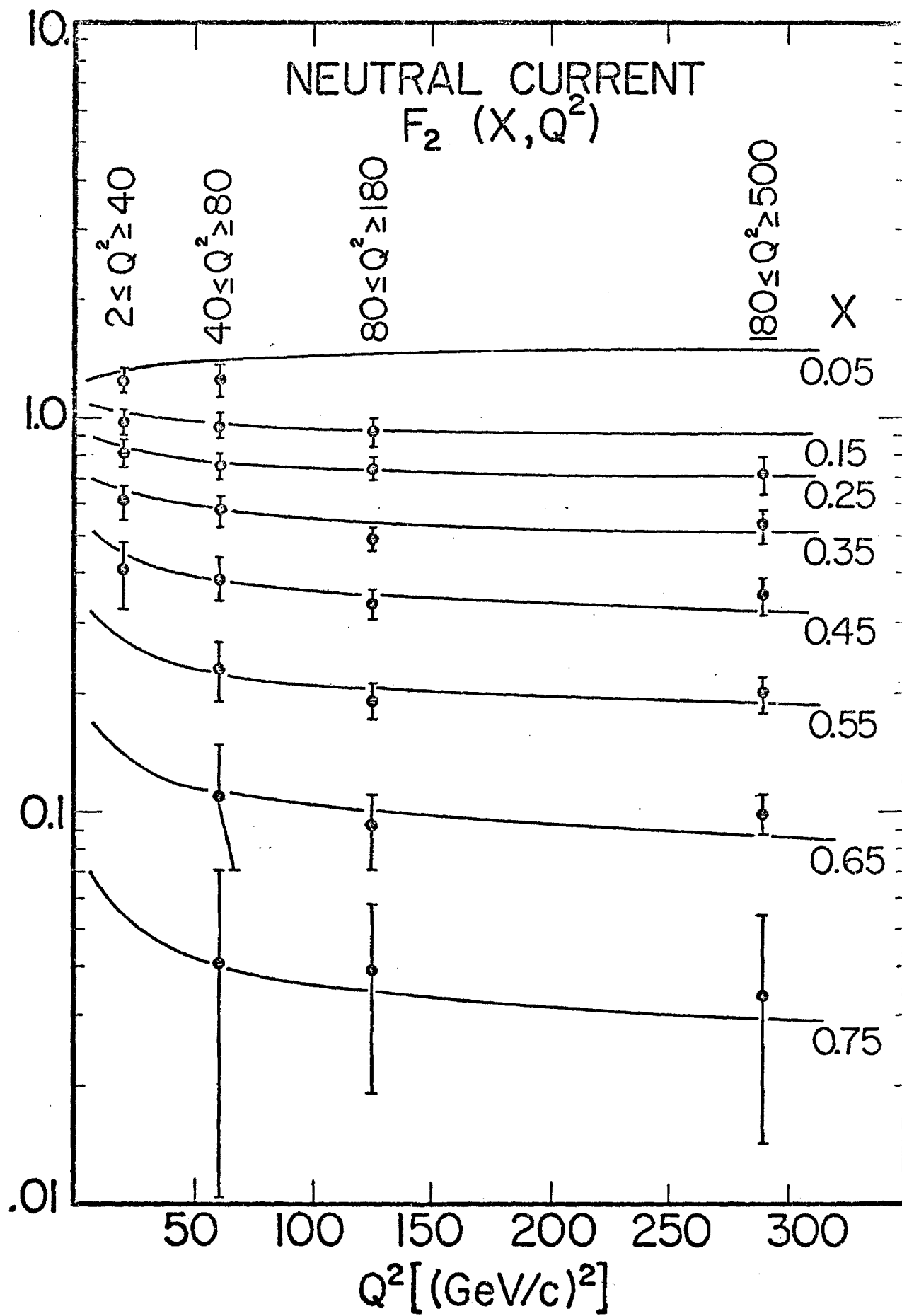


Figure 16

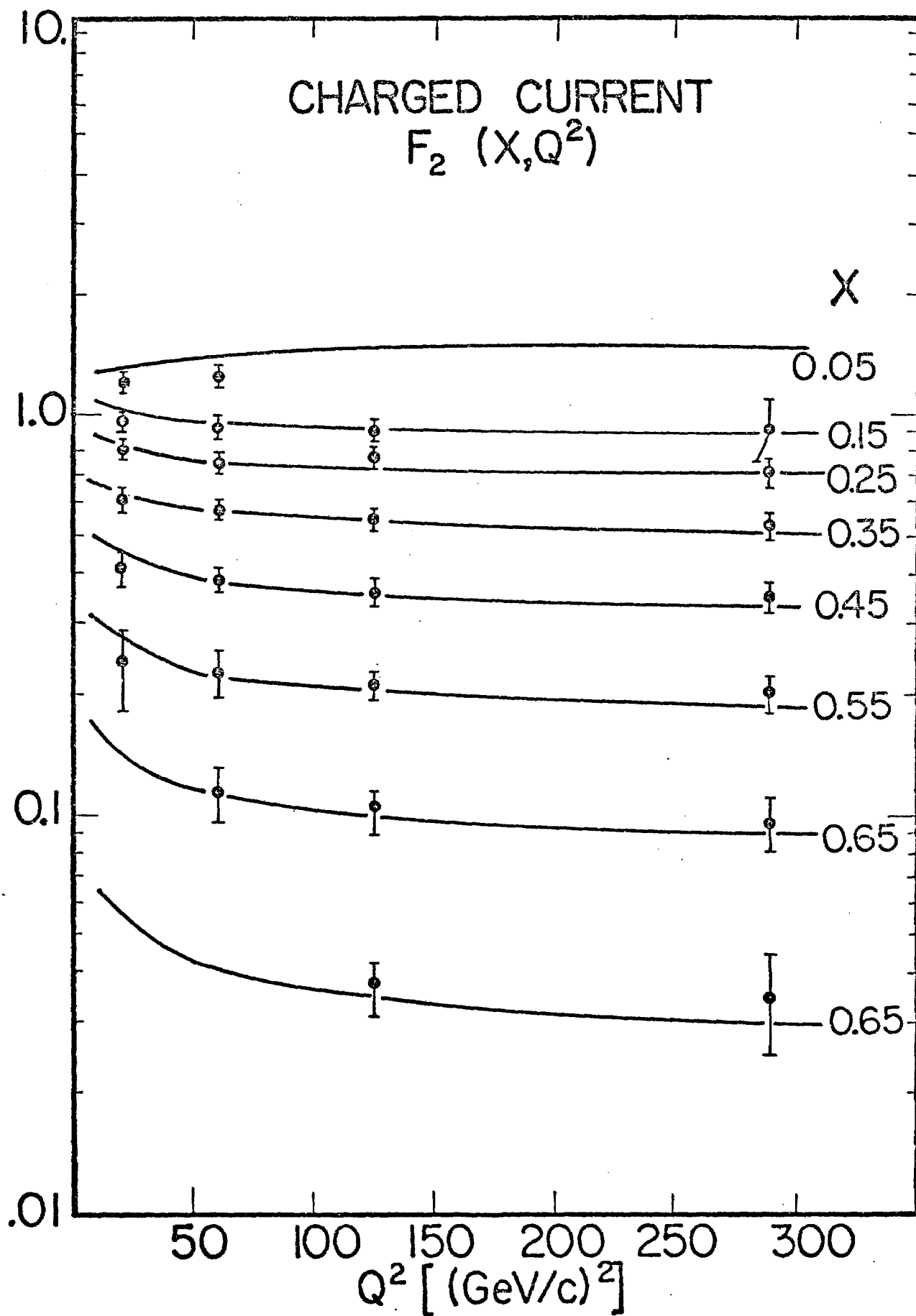


Figure 17

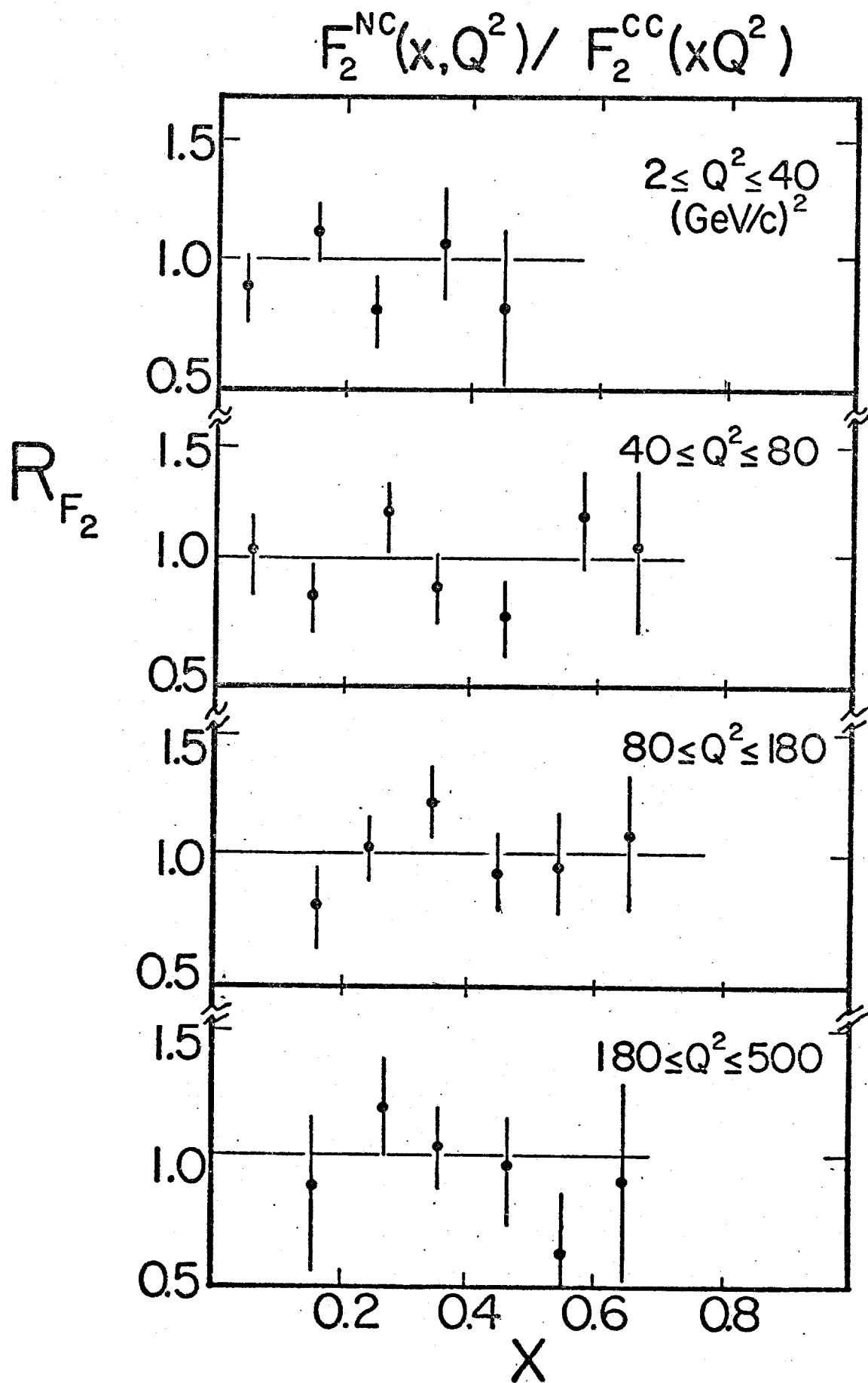


Figure 18

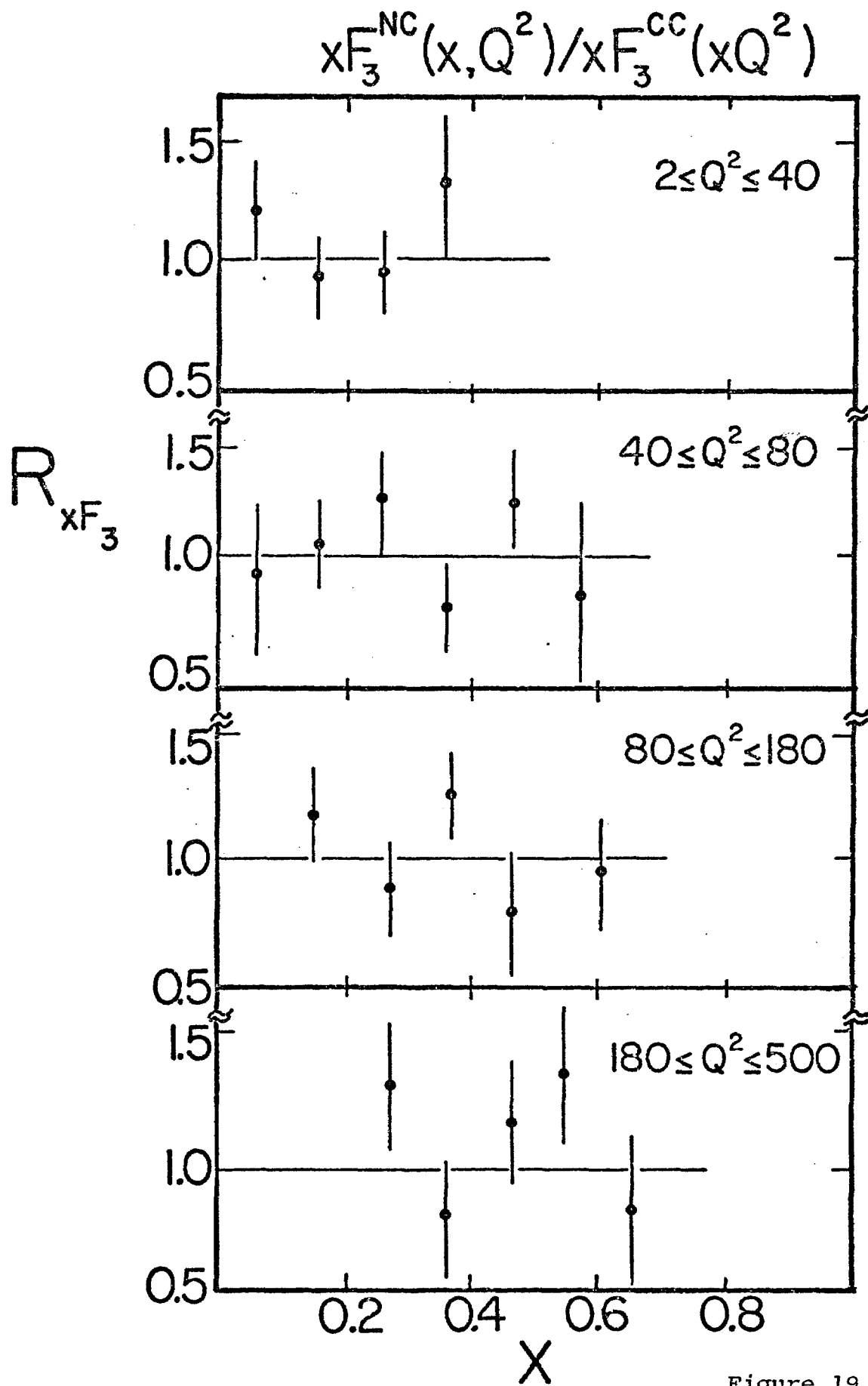


Figure 19

APPENDIX A: THE APPARATUS

I. INTRODUCTION

The Lab C flash chamber - proportional tube calorimeter is well suited for Tevatron era neutrino physics. It is ideal for studying neutral and charged current interactions, ν -e scattering and beam dump ν_τ physics. The calorimeter is fine grained (~400,000 flash tube cells) with a sampling step every 3% of an absorption length and 22% of a radiation length. It can distinguish electromagnetic from hadronic showers and has good energy and angular resolution for both. It has an excellent pattern recognition capability. Good muon momentum resolution at Tevatron energies is achieved by the 24' and 12' iron toroids which will be instrumented with drift chambers.

II. DESCRIPTION OF THE CALORIMETER

A. Arrangement of the Calorimeter

The flash chamber - proportional tube calorimeter is 60 feet (18 meters) long comprising 340 metric tons (see Fig. 1). The flash chambers are arranged in three views (X, Y and U) with cells which run 0° , 80° and 100° relative to horizontal (see Fig. 2). Each flash chamber is sandwiched by a sand plane and a steel shot plane. These target-absorber planes are made from extruded acrylic plastic sheets with $5/8"$ x $5/8"$ x 12' vertical cells filled with either sand or steel shot. Table I shows the arrangement of the target-absorber planes within the flash chambers and lists the corresponding absorption and radiation

lengths. The proportional tube planes are located one every 16 flash chambers. Hence between adjacent proportional planes are 0.5 absorption lengths (64 g/cm^2) or 3.5 radiation lengths. The proportional tubes are alternately vertical and horizontal.

B. General Properties

The average density of the calorimeter is 1.40 g/cm^3 . The average nuclear charge Z is 19.1. This low average Z was obtained by using sand as a part of our target-absorber and allows us to measure the angle of electromagnetic showers well. The average collision, absorption and radiation lengths in the calorimeter are 51.8, 83.1 and 11.7 cm respectively. The size of hadronic showers in the calorimeter, or more precisely the dimensions required for containment of the shower energy, is given in Fig. 4. The curves in Fig. 4 were obtained using shower depth calculations in liquid scintillator by the HPWF group.¹ The hadronic shower resolutions, discussed later, demand at least 99% of the shower is contained in the calorimeter longitudinally and at least 95% laterally. The calorimeter properties are summarized in Table II.

C. The Flash Chambers

There are about 600 flash chambers, each with approximately 650 5 mm x 5 mm cells. This fine granularity of the flash chambers allows a small sampling step of the recoil showers leading to excellent energy and angle determination, pattern recognition and muon track finding. The flash chambers are made

of extruded black polypropylene with aluminum foil electrodes glued on both sides. Each flash chamber has an active area of 12' x 12' (3.66 m x 3.66 m). Standard spark chamber gas: 90% Ne, 10% He, is circulated through the cells.

When an event is detected, a high voltage pulse of 4.5 kV is applied across each chamber for 0.5 μ sec. During this high voltage pulse, a plasma discharge is developed in the hit cells of the flash chambers. This plasma discharge propagates down the full 12' length of the flash chamber cell and into a read out region at the end of each cell. A copper strip for each cell is glued over this 2-ft long read out region and develops a current pulse when the cell is hit. The current pulse is then read out by magnetostrictive techniques.

D. The Proportional Tubes

The trigger and energy determination at large energies are provided by planes of proportional tubes. There are 37 such planes, each containing 144 tubes. The planes are made of extruded aluminum. Each tube is 1" x 1" x 12' and is strung with a single 2 mil gold plated tungsten wire. Four tubes are connected to one amplifier to reduce the cost of electronics while still maintaining adequate granularity for triggering purposes. An argon-ethane (50%-50%) gas mixture is used to give fast drift times (≤ 200 ns) needed to form the trigger within the flash chamber sensitive time.

The trigger will be based on the total energy deposition and on the topology of the energy deposition. Discrimination

in the trigger between electromagnetic and hadronic showers will be accomplished using the shower length (the number of proportional planes hit) and the shower width (the separation of hit channels within a plane).

E. Scintillation Counters

Liquid scintillation counters with a 12' x 12' sensitive area are placed every 80 flash chambers throughout the calorimeter. The most upstream counter serves as a front wall veto counter. The other scintillation counters will be used for efficiency measurements and corroborative information on hadronic shower energy deposition. They will also provide time of flight information.

F. The Muon Spectrometer

The muon momentum for charged current interactions and multi-muon events will be measured in the muon spectrometer at the rear of the apparatus (see Fig. 1). There are three 24-ft diameter by 2-ft thick iron toroids immediately downstream of the calorimeter and four 12-ft diameter by 4-ft thick iron toroids behind these. The muons travel through the equivalent of approximately 13 kG in 5 meters of magnetized iron, corresponding to a p_{\perp} kick of about 2 GeV/c.

The toroids are instrumented with scintillation counters to supply trigger information regarding the presence or absence of a muon in the toroids. Behind each of the seven toroids will be four planes of drift tubes. The planes are made of

extruded aluminum, each tube having a 1" x 1" cross section. Two of the four planes will have vertical tubes: the tubes of one plane being offset one-half of a tube with respect to those of the other plane to resolve right-left ambiguities. The other two planes of the set of four will have horizontal tubes.

III. RESOLUTIONS

A. Energy Resolution

The hadronic shower energy is measured by the flash chambers at low energies and the proportional tubes at high energies (see Fig. 4). Because of their fine grained sampling, the flash chambers provide good resolution as low as 10 GeV. At high energies (above 200 GeV), where multiple hits per cell degrade the flash chamber resolution, the proportional tubes provide a good energy measurement. Figure 5 shows the electromagnetic shower energy resolution determined only by the flash chambers. For both kinds of showers, the flash chamber energy measurement is determined by cell counting. The proportional tube energy measurement is determined by summing the analog signals from all the wires.

The preliminary flash chamber energy resolutions in Figs. 4 and 5 were directly measured in a hadron and electron beam using our test calorimeter.² The test calorimeter was made with plastic flash chambers, smaller in size and number than our Lab C chambers, and read out optically. The longitudinal sampling of the test calorimeter: $3.5\% \lambda_{\text{abs}}$ and $24\% X_0$, was almost as good as

the Lab C calorimeter. Therefore only corrections for the limited hadronic shower containment of the test calorimeter were made to the measured resolutions. The proportional tube resolution of Fig. 4 was estimated by scaling Anderson et al.³ to our sampling step, giving

$$\frac{\sigma(E_h)}{E_h} \approx \frac{104\%}{\sqrt{E_h}}$$

B. Angular Resolution

The hadronic and electromagnetic shower angular resolutions determined by the test flash chamber calorimeter are shown in Figs. 6 and 7. The angular resolutions depend critically on the spatial resolution of the shower vertex. The angle of the showers is computed by first locating the vertex and then using the "center of gravity" of the shower as a function of shower depth.

Because every cell of the test calorimeter ran horizontal, the sampling step per view was approximately a factor of two finer in the test calorimeter than in the Lab C calorimeter. By ignoring every other plane in the test calorimeter's angle measurement, therefore, we were able to plot the expected angular resolution of the Lab C calorimeter. The test calorimeter confirmed the expectation of good angular resolution at low energies: an important feature for beam dump physics. Figure 8 shows test calorimeter showers at all energies. Note the good vertex determination even at low energies.

C. Pattern Recognition

We will be able to distinguish electromagnetic from hadronic showers by their size, shape and structure. This is an important capability for the study of ν -e scattering where hadronic backgrounds are large. As seen in the test calorimeter showers of Fig. 8, electromagnetic showers are easily distinguished from high energy hadronic showers by differences in their size. We distinguish low energy hadronic from electromagnetic showers by the presence of large angle secondaries in the hadronic showers. Also, unlike electromagnetic showers, tracks are visible within the hadronic showers. Using the test calorimeter in a hadron beam with about 1% electron contamination, we were able to experimentally confirm that less than 1% of hadron showers are misidentified as electron showers.

We will also be able to observe and locate the muon track in charged current interactions. We expect a very small amount of charged current interactions posing as neutral current interactions because the muon could not be seen.

D. Muon Momentum Resolution

Figure 9 shows the muon momentum resolution we expect to achieve when the 24 and 12-ft iron toroids are instrumented with drift tubes. The drift tubes will provide position measurements with an estimated σ of 1 mm. The flash chambers will supply information regarding the muon's trajectory at the point of entry into the first toroid. The resolutions corresponding to the drift tube and flash chamber position measurements, as well as multiple scattering were used to produce the resolution shown.

IV. PERFORMANCE OF THE CALORIMETER

A. Flash Chamber Performance

We have debugged and operated 320 flash chambers. From our experience we find that the flash chambers have performed well.⁴ Using cosmic ray muons, we have measured their efficiency at the proportional tube trigger time delay (650 ns from the event to the time high voltage appears across the chambers) to be between 80 and 90%. The multiplicity (cells lit per flash chamber per cosmic ray) is 1.3. Adequate recirculation of the neon-helium gas was found to be 1.5% of the volume per minute. For the entire detector, this implies a recirculation rate of 900 liters per minute. The high voltage plateau region is broad: 3.5 to 5.5 kV (see Fig. 10). The signal-to-noise ratio of the amplified signals on the magnetostrictive lines is 10:1. Our maximum repetition rate with almost no cell reignition thus far is ~1 flash per second. We have not added any electronegative gas to try to improve this.⁵ The readout dead time (up to the computer) is ~70 ms. Because data transfer time to the disk is 50,000-80,000 words per second, the computer cannot handle much more than one event per second. If we wanted to take data at a faster rate, we could transfer data without the disk by obtaining much more addressable core memory (such as a VAX) or by using a 6250 BPI tape drive.

Figure 11 shows a cosmic ray muon in 160 of our chambers. (Offline alignment corrections have not yet been made.) In Fig. 12, a cosmic ray muon initiated an electromagnetic shower. In Fig. 13, which shows a cosmic ray muon interacting, 320 of our chambers were in operation.

B. Proportional Tube Performance

The proportional tubes have also performed well. Using 50% argon - 50% ethane gas and running at a high voltage of 2000 volts gives us a gas gain of about 2000 and drift times of $\lesssim 200$ ns. The amplifier gain is 1 mV/fC. A minimum ionizing particle gives a signal of 8 mV: a factor of 8 above noise. The linear swing is 0-4 volts or 0-500 particles. This is a factor of 2 or so above the largest number of particles per channel expected for Tevatron energy showers. The tube to tube uniformity has been measured to be very good: a plot of Cd^{109} peaks for a large sample of tubes shows a σ of $\lesssim 5\%$.

V. CONCLUSION

The flash chamber - proportional tube calorimeter is a high tonnage, fine grained device with good energy and angle resolutions for both hadronic and electromagnetic showers. It has a good hadronic-electromagnetic shower distinction capability and a low average Z , making it ideal for the study of ν -e scattering. Its good vertex determination and good muon momentum resolution make it ideal for studying charged and neutral current interactions. Its good pattern recognition and angle determination at low energies make it an excellent beam dump detector. It will be a powerful device for studying a number of interesting physical processes at Tevatron energies.

REFERENCES

1. F. J. Sciulli, Proceedings of the Calorimeter Workshop (Fermilab), 79 (1975).
2. See Appendix A of the E594 Proposal (February 1978) and F. E. Taylor et al., IEEE Trans. Nucl. Sci. NS-25, 312 (1978).
3. R. L. Anderson et al., IEEE Trans. Nucl. Sci. NS-25, 340 (1978) and private communication with D. M. Ritson.
4. F. E. Taylor et al., IEEE Trans. Nucl. Sci. NS-27, 30 (1980).
5. Chaney and Breare, by adding 1% methane to the neon-helium, have been able to pulse their flash chambers at 50 Hz with no reignition. See J. E. Chaney and J. M. Breare, Nucl. Instrum. and Methods 124, 61 (1975).

TABLE I

Arrangement of Calorimeter Components

flash chambers:	U	X	Y	X	.	.	.
	↑	↑	↑	↑			
absorber planes:	shot	sand	shot	sand			
absorption lengths:	3.7%	2.5%	} 6.1% per view (7.2 g/cm ²)				
radiation lengths:	36%	8%	} 44% per view				

TABLE II

General Properties

Tonnage:	340 metric tons
Fiducial Tonnage for a Neutral Current Experiment:	100 metric tons
Fiducial Tonnage for a ν -e Scattering Experiment:	225 metric tons
Average Density:	1.40 g/cm ³
Average Z:	19.1
Average λ_{COL} :	51.8 cm
λ_{ABS} :	83.1 cm
X_{O} :	11.7 cm

LIST OF FIGURES

- Fig. 1a Top View of Apparatus
- Fig. 1b Recent Photograph of Apparatus
- Fig. 2 Arrangement of the Flash Chambers
- Fig. 3a Length of Calorimeter Needed to Contain 99% (or 90%)
 of the Shower
- Fig. 3b Radius of Calorimeter Needed to Contain 99% (or 95%)
 of the Shower
- Fig. 4 Hadron Energy Resolution
- Fig. 5 Electron Energy Resolution
- Fig. 6 Hadron Angular Resolution (projected angle)
- Fig. 7 Electron Angular Resolution (projected angle)
- Fig. 8 Test Calorimeter Electromagnetic and Hadronic Showers
- Fig. 9 Muon Momentum Resolution with the Drift Tube
 Instrumented Toroids
- Fig. 10 Efficiency vs. HV for the Flash Chambers
- Fig. 11 Cosmic Ray Muon in 160 Flash Chambers
- Fig. 12 Cosmic Muon Induced Electromagnetic Shower in
 160 Flash Chambers
- Fig. 13 Interaction of Cosmic Ray Muon in 320 Flash Chambers

E-594 CALORIMETER

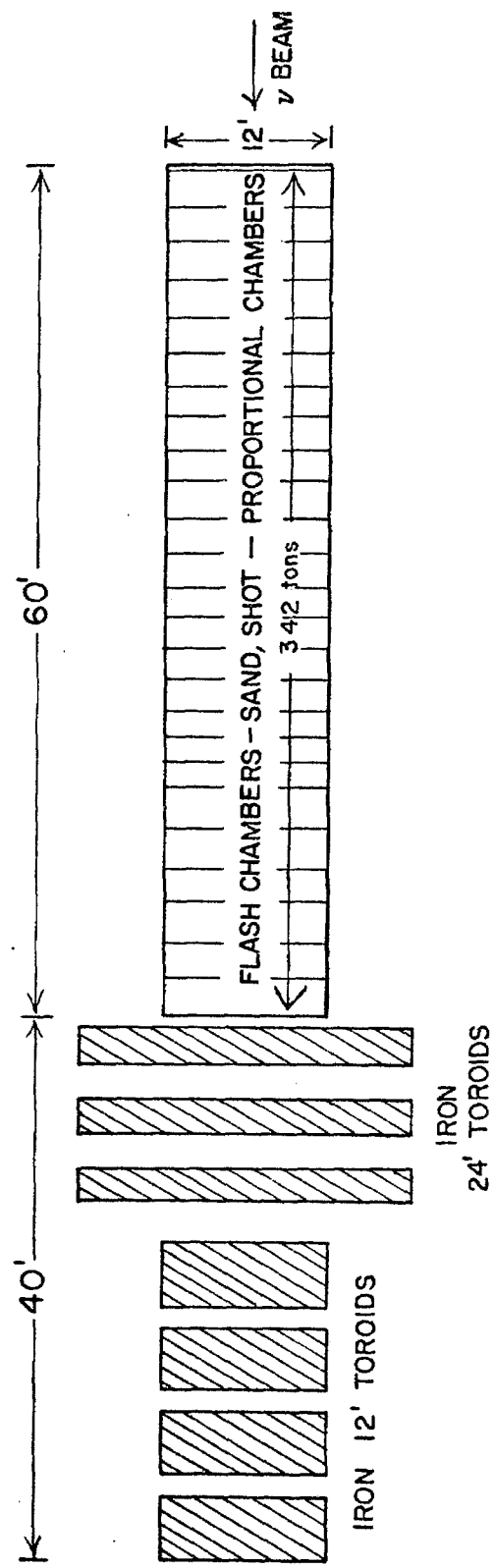


Figure 1a



Figure 1b

FLASH CHAMBER CALORIMETER CONSTRUCTION

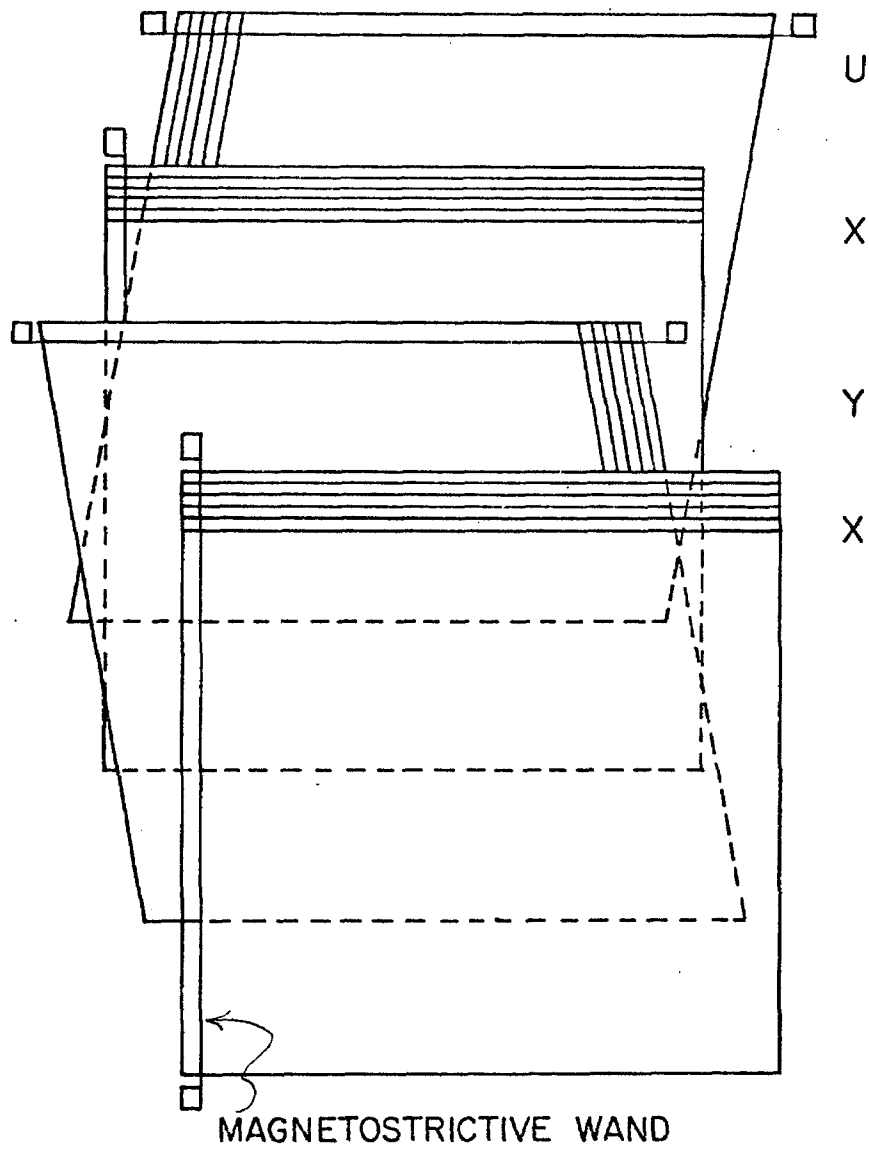


Figure 2

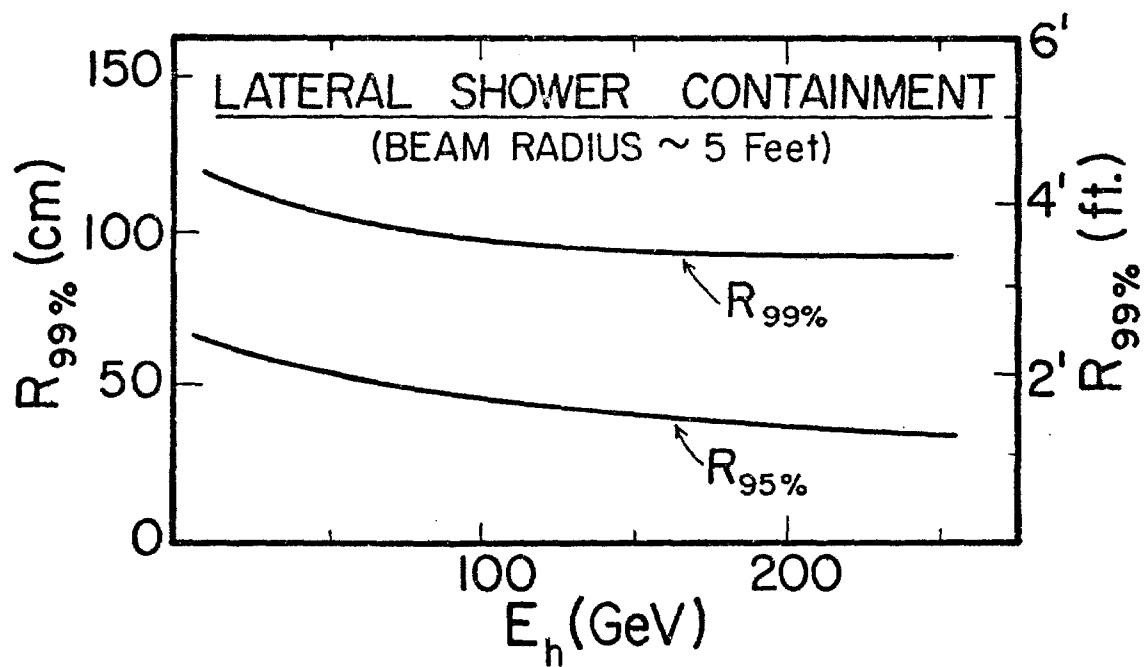
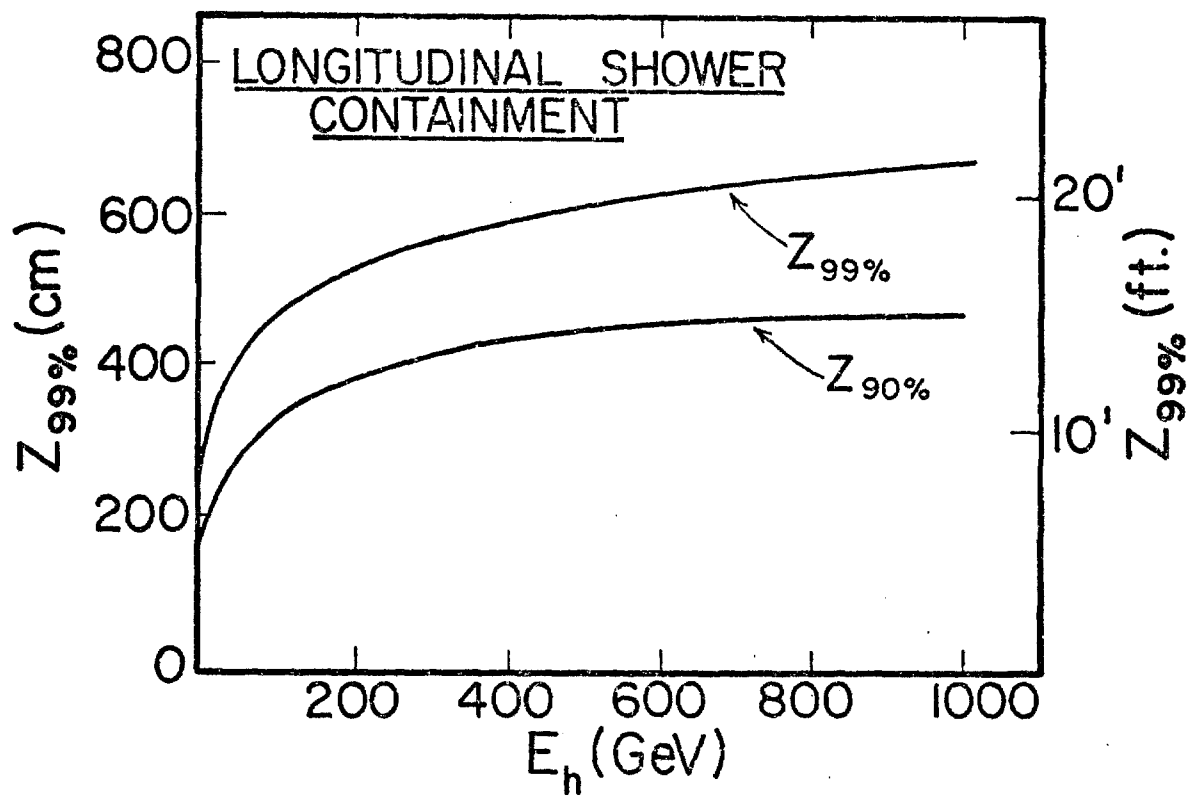


Figure 3

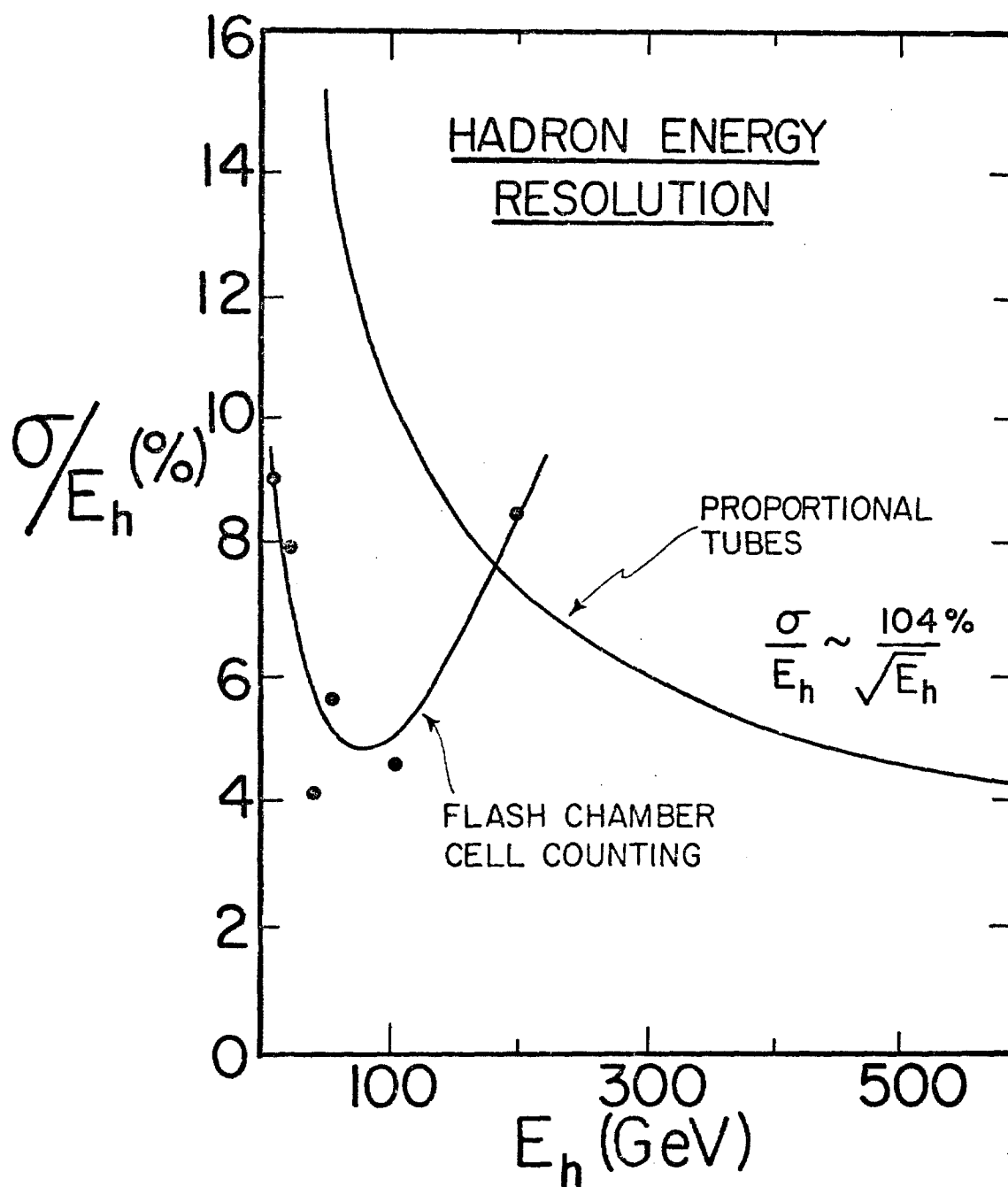


Figure 4

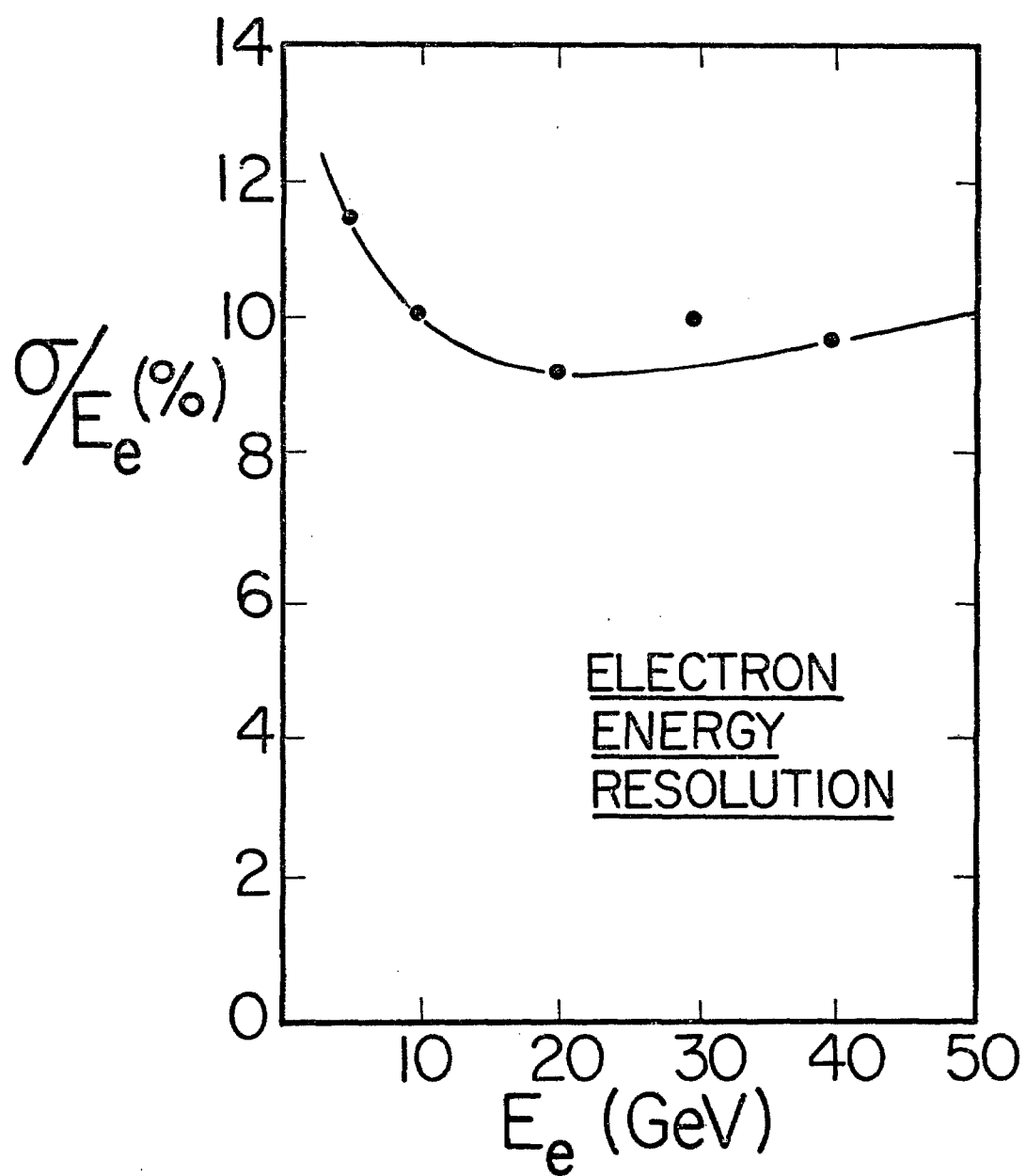


Figure 5

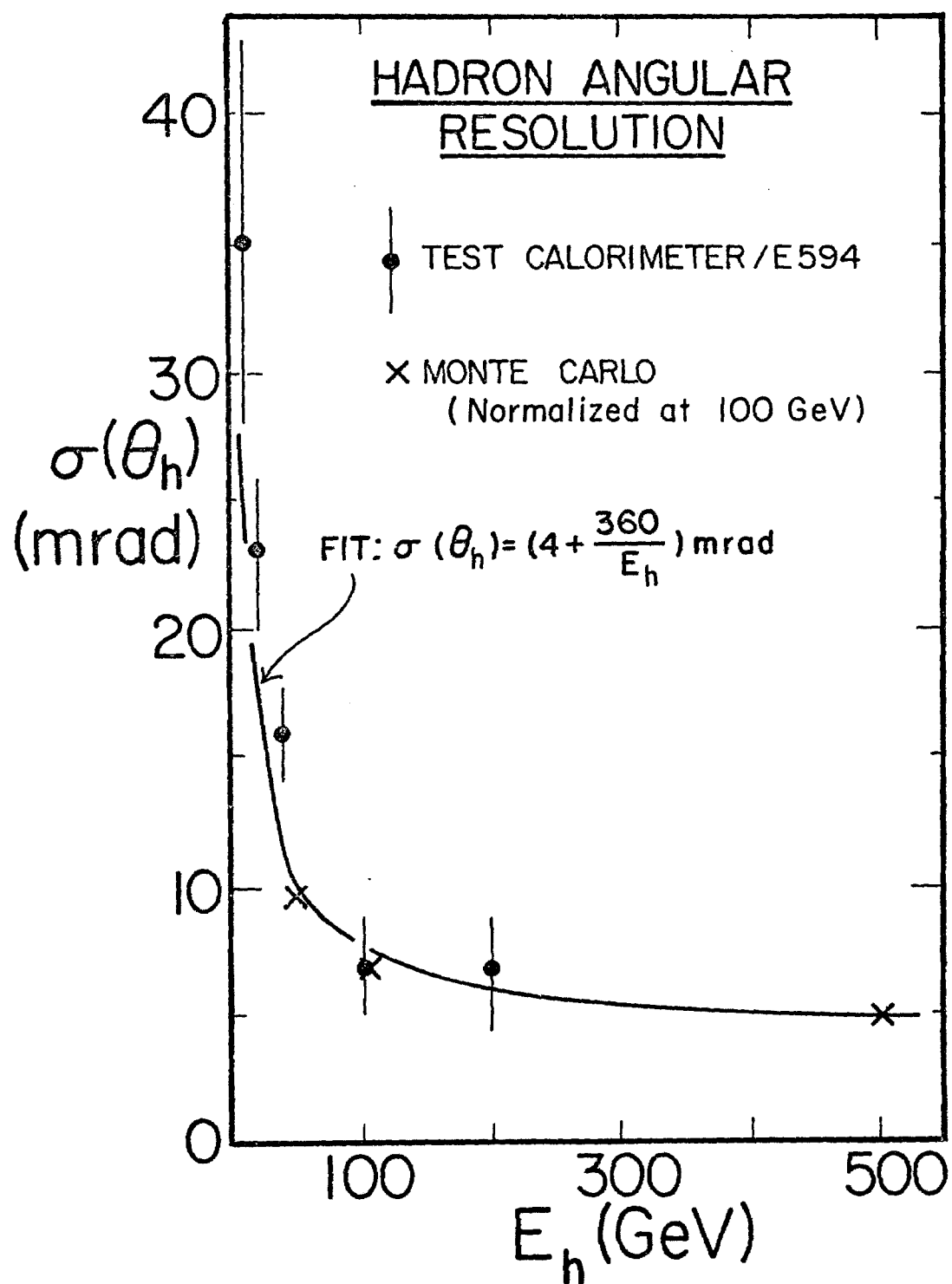


Figure 6

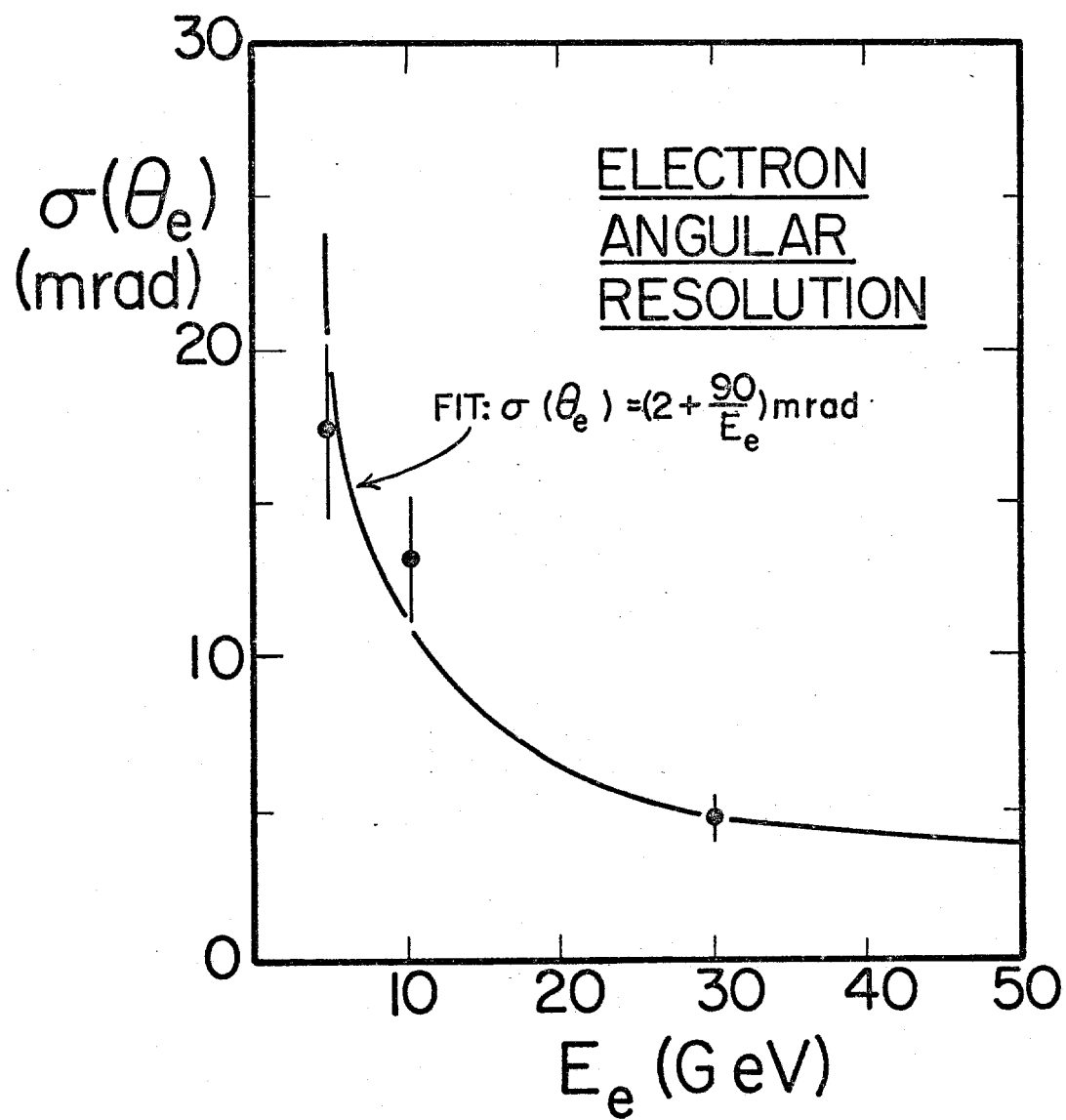
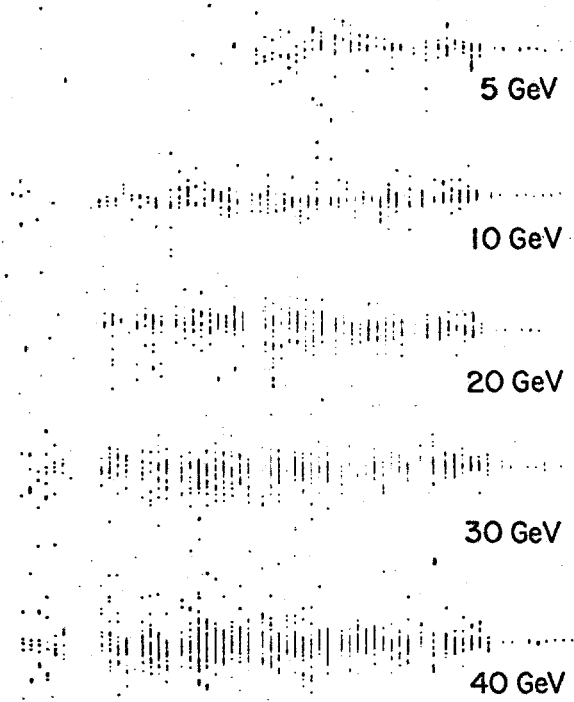


Figure 7

ELECTRON SHOWERS

TEST CALORIMETER SHOWERS



HADRON SHOWERS

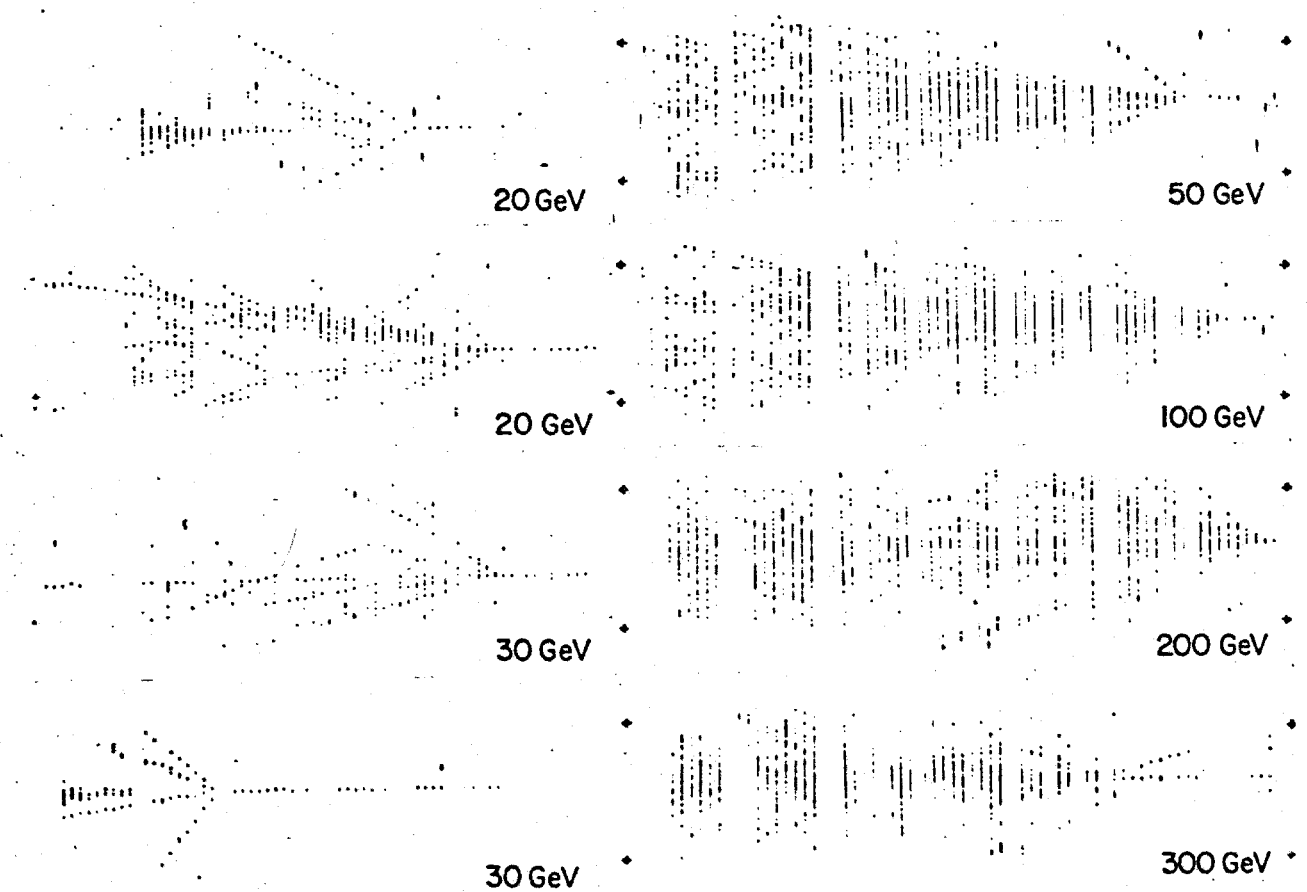


Figure 8

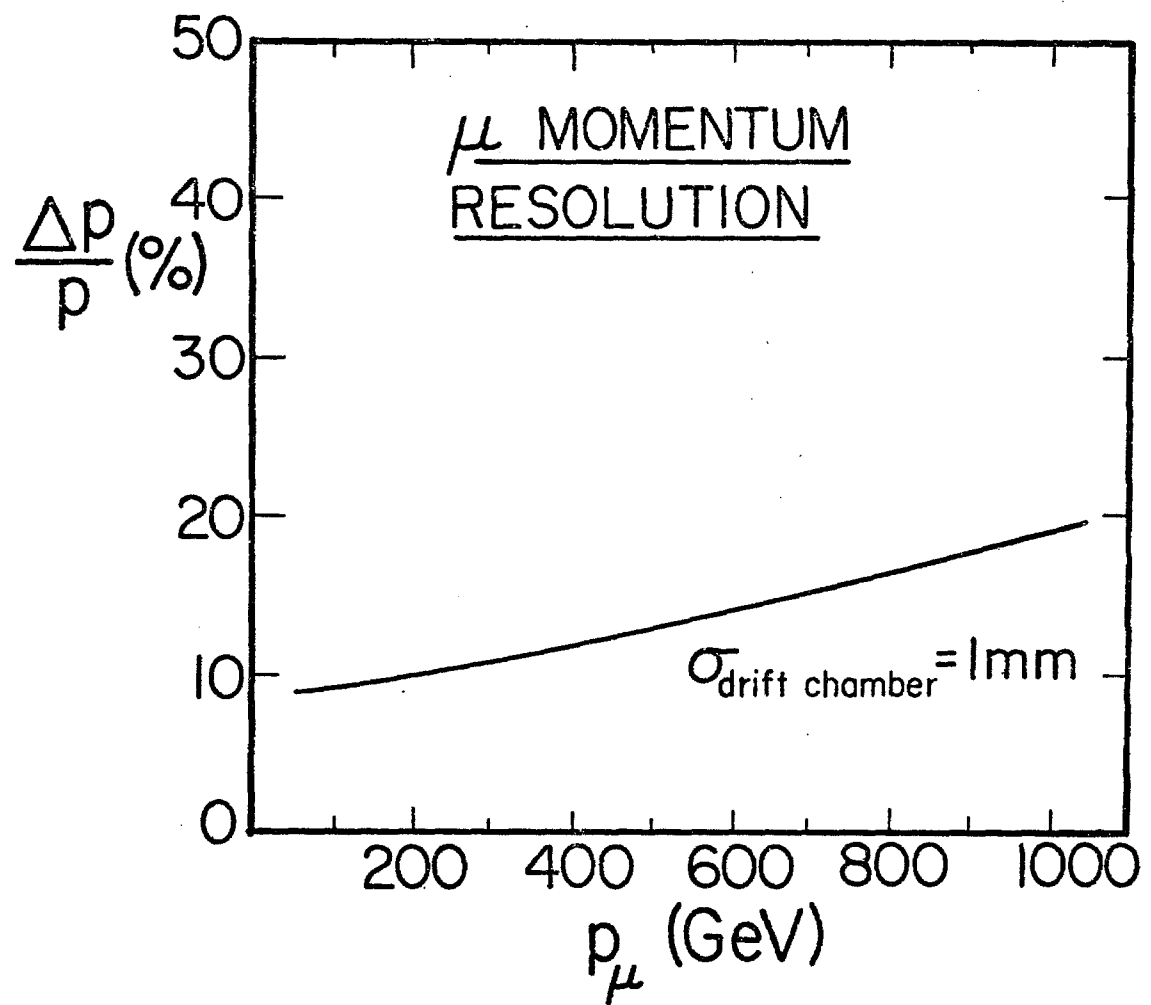


Figure 9

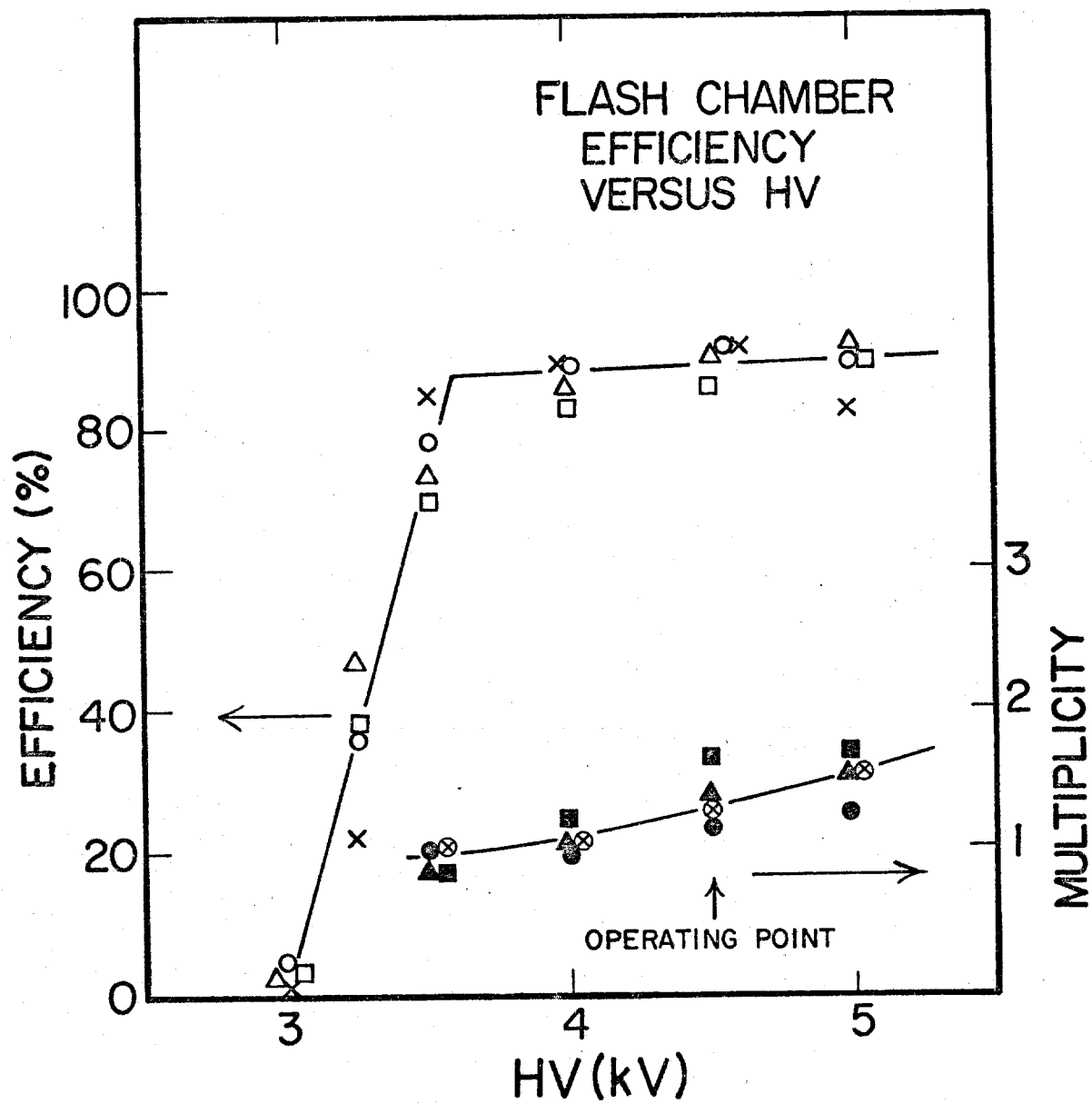
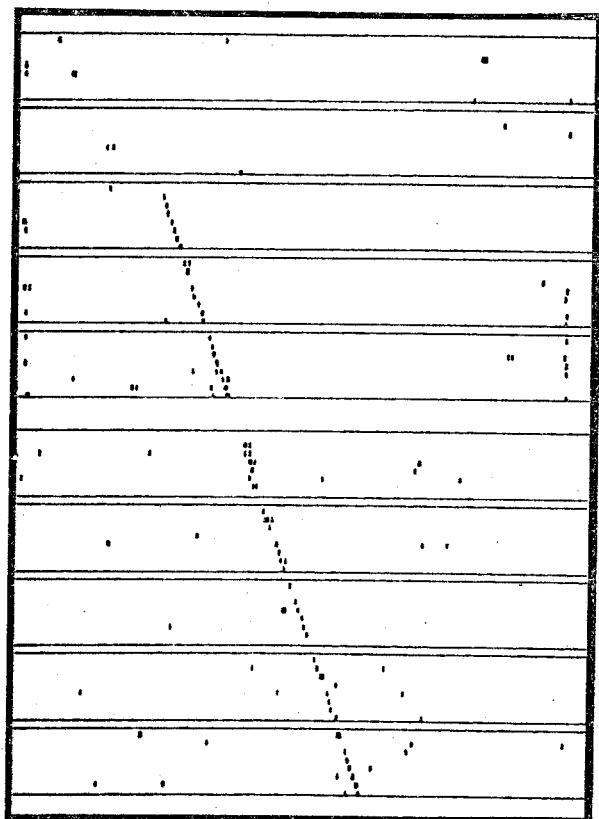
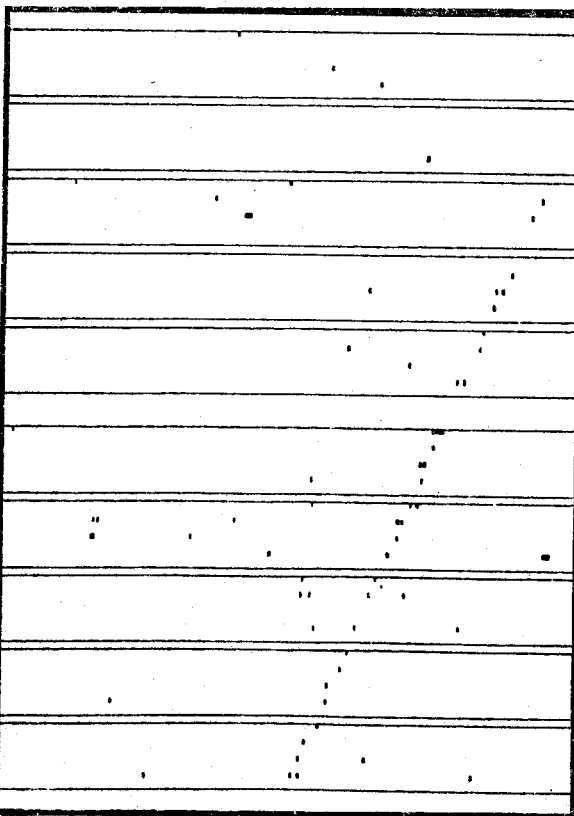


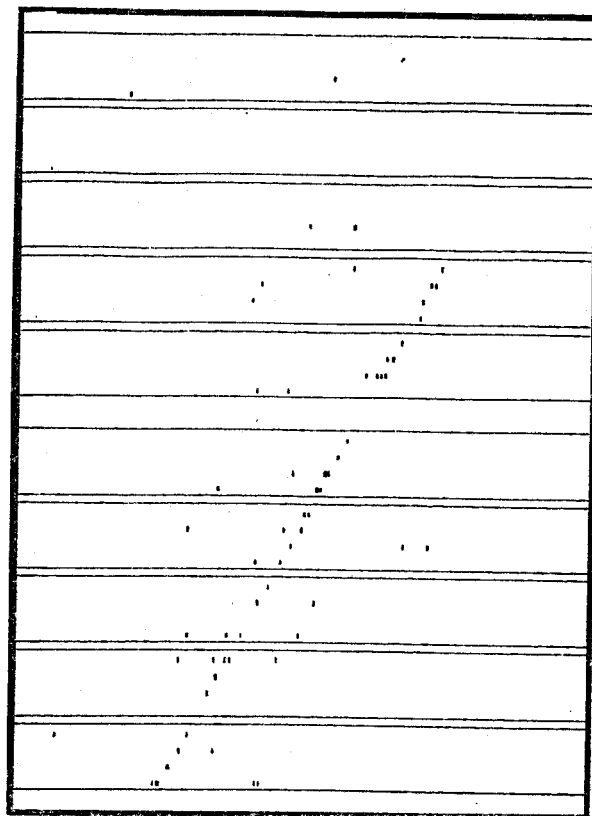
Figure 10



X VIEW



U VIEW



Y VIEW

Figure 11

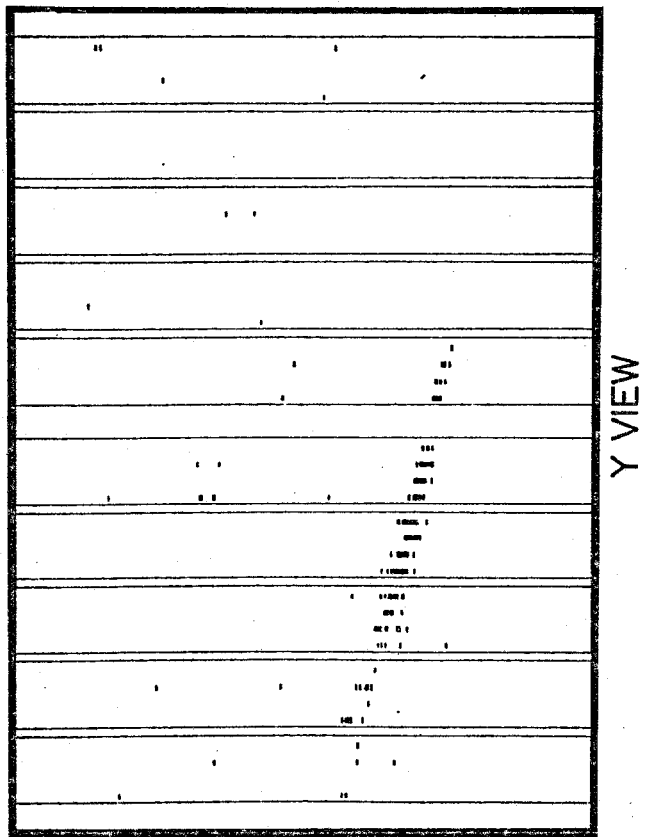
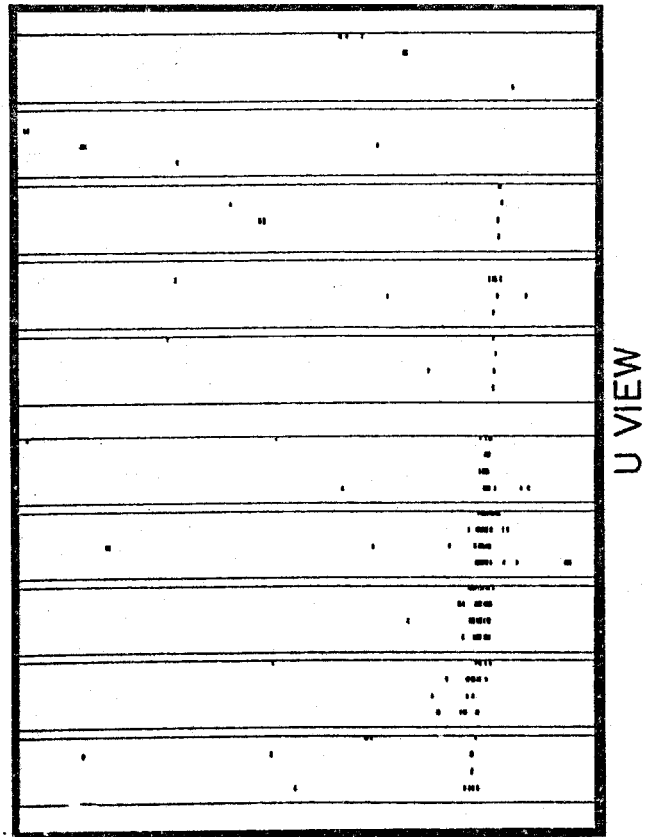
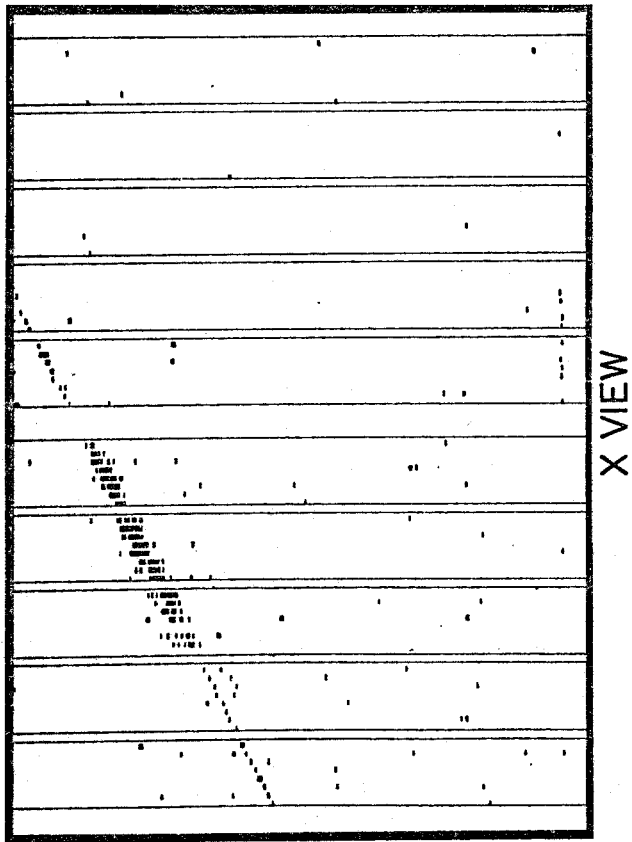


Figure 12

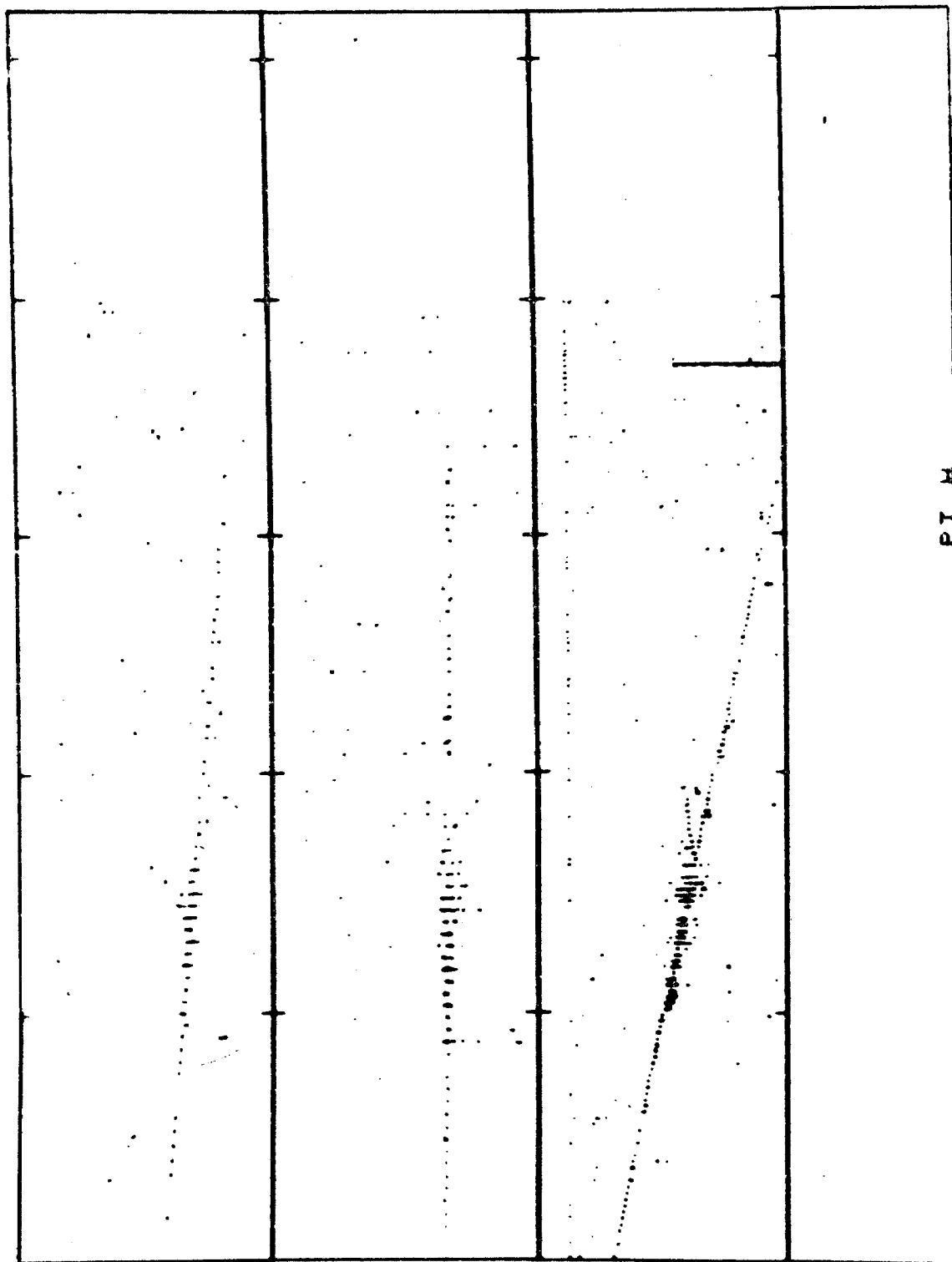


Figure 13